Department of Physics and Astronomy
Heidelberg University

Master Thesis

in Physics

submitted by

Ansgar Lowack

born in Gladbeck, Germany

2021

Development of a 4k pixel detector array for the energetically, temporally and spatially resolved detection of neutral molecule fragments with kinetic energies up to 300 keV

This Master thesis has been carried out by
Ansgar Lowack
at the
Kirchhoff-Institute for Physics
under the supervision of
Prof. Dr. Christian Enss

This thesis presents a new detector design for the simultaneous energy-, time- and spatially-resolved detection of neutral molecule fragments with kinetic energies up to 300 keV. The detector will be used at the Max-Planck-Institute for Nuclear Physics in Heidelberg to study dissociative recombination reactions. The detector is based on metallic magnetic calorimeters (MMCs). These are low-temperature detectors in which a metallic absorber is thermally coupled to a high-precision paramagnetic temperature sensor. The kinetic energy of a particle hitting the absorber is converted into heat which is then measured as a change in temperature. The detector developed achieves high spatial resolution by combining 64×64 MMCs on a detector area of $4.48\,\mathrm{cm} \times 4.48\,\mathrm{cm}$. This is enabled by a new readout scheme which reduces the resulting 4096 pixels to just 32 SQUID channels. For this purpose, the spatial information on where the particle was absorbed on the detector surface is encoded in the polarity, decay time and channel number of the measurement signal. Simulations yield an expected intrinsic energy resolution of the detector of $E_{\mathrm{FWHM}} \approx 40\,\mathrm{eV}$. The design and upcoming fabrication of the detector are discussed, with particular emphasis on advances in the fabrication of gold-filled holes through silicon wafers.

Entwicklung eines 4k Pixel Detektorarrays für die energie-, zeit- und ortsaufgelöste Detektion neutraler Molekülfragmenten mit kinetischen Energien von bis zu 300 keV

Im Rahmen der vorliegenden Arbeit wird ein neues Detektordesign zur gleichzeitigen energie-, zeit- und ortsaufgelösten Detektion neutraler Molekülfragmente mit Energien von bis zu 300 keV vorgestellt. Der Detektor soll am Max-Planck-Institut für Kernphysik in Heidelberg bei der Untersuchung dissoziativer Rekombinationsreaktionen eingesetzt werden. Der Detektor basiert auf metallischen magnetischen Kalorimetern (MMCs). Hierbei handelt es sich um Tieftemperaturdetektoren, bei denen ein metallischer Absorber thermisch an einen hochpräzisen paramagnetischen Temperatursensor gekoppelt ist. Trifft ein Teilchen den Absorber, wandelt es seine kinetische Energie in Wärme um, die dann als Temperaturänderung gemessen wird. Der entwickelte Detektor erreicht eine hohe räumliche Auflösung, indem er 64×64 MMCs auf einer Detektorfläche von $4.48\,\mathrm{cm} \times 4.48\,\mathrm{cm}$ miteinander kombiniert. Ermöglicht wird dies durch ein neues Ausleseschema, bei dem die resultierenden 4096 Pixel mit lediglich 32 SQUID-Kanälen ausgelesen werden. Hierzu wird die räumliche Information darüber, wo das Teilchen auf der Detektorfläche absorbiert wurde, in der Polarität, Abklingzeit und Kanalnummer des Messsignals kodiert. Simulationen ergeben eine erwartete intrinsische Energieauflösung des Detektors von $E_{\mathrm{FWHM}} \approx 40\,\mathrm{eV}$. Die Arbeit geht auf Design und die anstehende Fabrikation des Detektors ein, wobei insbesondere Fortschritte in der Fabrikation goldgefüllter Löcher durch Silizium Wafer präsentiert werden.

Contents

1. Introduction

Interstellar clouds of atoms and molecules are vast assemblages of matter in space at typical temperatures and particle densities below 10 K and 200 particles/cm^3 [Tie05]. Although one would hardly expect the formation of large molecules under such extreme conditions, the chemistry of interstellar clouds is surprisingly divers [McG18]. Starting about 80 years ago with the detection of CH and CN, today over 200 different molecules have been spectroscopically identified in them, including even complex ones such as ethanol, acetone or Buckminsterfullerenes (e.g. C_{60}) [Zha11, Cam10]. Moreover, many absorption bands already measured are still of unknown origin, especially since the exact processes responsible for molecule formation at low temperatures and pressures are not well understood. One such process is the dissociative recombination of positively charged molecular ions with electrons and their subsequent decay into neutral molecule fragments. This enables the formation of radicals which might combine into large and complex molecules. Since this process is exothermic with low activation energy, it is very efficient even under the conditions in interstellar clouds where most other chemical mechanisms only work very slowly or not at all.

More experimental data is needed to extend the theoretical understanding of dissociative recombination. To this end, the ambient conditions of interstellar clouds are emulated in the Cryogenic Storage Ring (CSR) of the Max-Planck-Institute for Nuclear Physics in Heidelberg. Here, a beam of ionized molecules can be stored at energies between 20 and 300 keV on a 35 m circumference orbit and cooled to temperatures below 10 K at densities below 140 particles/cm^3. The ion beam can be superimposed with a nearly mono-energetic, velocity-controlled electron beam, enabling phase-space cooling of ions into their rotational and vibrational ground states. Subsequently, these molecule ions can be recombined with the electrons which may lead to their decay into neutral molecule fragments. Since neutral particles are not held by the ring's electromagnetic fields, they hit an appropriately positioned detector. To understand the reactions inside the ring, the detector should be able to measure the kinetic energy, impact time, and position of all incident products over a large enough area.

However, with the detectors currently in use, only either energy- or spatially-resolved measurements of massive neutral particles are possible simultaneously with sufficient precision. A new approach to solve this problem is the use of MMC based low temperature detectors which have already been used over a wide range of applications [Hen17, Vel19, Gei20, Sik20]. This is a class of low temperature detectors in which a

metallic absorber is thermally connected to a magnetized paramagnetic temperature sensor. An energy input into the absorber thus leads to a temperature increase in the sensor. Consequently, the entropy gain of the paramagnetic spin system results in a decrease of the magnetization. This change is coupled into a superconducting detection coil and converted into a measurable voltage signal using a SQUID. Due to their caloric measurement principle MMCs are well suited for the detection of neutral massive particles. They combine excellent energy resolutions with fast signal rise times and are linear over a broad energy range [Fle09]. The first prototype developed for this purpose in [Gam19] and [Sch21] is the molecular camera "MOCCA" which combines an energy resolution of about 90 eV with a spatial resolution of 4096 pixels on a 4.48 cm × 4.48 cm detection area. However, this detector is exceptionally difficult to manufacture, a fact owed to the complexity of its design. In addition, MOCCA's time resolution is intrinsically limited to about 16 μs which may be insufficient for the planned measurements at CSR.

Therefore, a new detector was conceptualized in this thesis for the same purpose. It will be fabricated on a 3 inch silicon wafer and features an array of 64 × 64 individual MMC pixels, covering a detection area of 4.48 cm × 4.48 cm with a filling factor of 99.4 %. The resulting 4096 pixels are read out with only 32 SQUIDs by encoding the spatial information in the polarities, decay times and channel numbers of the MMC signals. This new readout scheme which is developed in this thesis, facilitates a reduction of design complexity compared to MOCCA. This allows easier fabrication, without limiting the theoretical temporal resolution to more than 1 μs. The only remaining design aspect that is critical from a manufacturing perspective is a total of 1024 gold-filled holes through the 380 μm thick silicon substrate of the detector chip, each 300 μm in diameter. However, this feature is only necessary for experiments with high rates of incoming particles. It was made feasible as part of this thesis by a further optimization of the deep etching of silicon using the Bosch process. Numerical simulations result in an expected intrinsic energy resolution of the detector of $E_{\mathrm{FWHM}} \approx 40\,\mathrm{eV}$.

This thesis is structured as follows: Chapter 2 provides an introduction to the operation principles of MMCs and briefly summarizes some of the physics necessary to understand the detector. In chapter 3, the detector design and the new readout scheme are discussed. Chapter 4 offers an overview of the fabrication steps required to produce the detector chip with details on the manufacture of gold-filled holes through the wafer. Finally, the thesis concludes with a summary of the main points and an outlook on the the future of the project in chapter 5.

2. Physical Fundamentals

This chapter summarizes the physical fundamentals required for a general understanding of the detector designed in this thesis. The working principles of metallic magnetic calorimeters (MMCs) are discussed, including the right choice of sensor material, SQUIDs and some low temperature specific solid state properties necessary to understand the operation of the detector.

2.1 Metallic magnetic calorimeters

The detector described in this thesis is based on metallic magnetic calorimeters (MMCs). The schematic structure of such a detector is shown in figure 2.1.

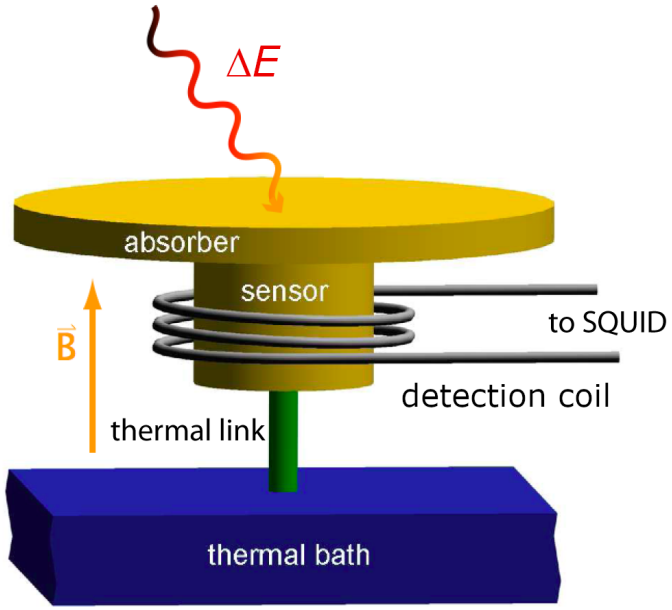

Figure 2.1: Schematic structure of a metallic magnetic calorimeter with energy input ΔE. A metallic absorber is thermally coupled to a paramagnetic sensor which is magnetized inside an external magnetic field **B**. The sensor in turn is linked to a thermal bath and is inductively coupled to a SQUID via a superconducting detection coil. Figure modified from [Sch21].

It consists of a metallic absorber which is strongly thermally coupled to a paramagnetic sensor, magnetized by an external magnetic field **B**. The sensor in turn is weakly linked to a heat bath. If an incoming particle hits the absorber, it deposits

an energy ΔE inside it. In the case of X-ray photons this energy corresponds to the photon energy $\Delta E = E_{\text{photon}}$ and in the case of massive particles to the kinetic energy $\Delta E = E_{\text{kin}}$ of the particles. While a loss-free energy measurement of X-ray photons is possible, the absorption of massive particles involves loss mechanisms which are briefly discussed in section 2.5. The energy input into the absorber leads to a local rise in temperature which spreads diffusively to the sensor. The resulting temperature change ΔT can be calculated in linear approximation as

$$\Delta T = \frac{\Delta E}{C_{\text{tot}}}\,, \tag{2.1}$$

assuming a weak thermal coupling to the heat bath. Here the total heat capacity $C_{\text{tot}} = C_{\text{a}} + C_{\text{s}}$ is the sum of the heat capacities C_{a} and C_{s} of the absorber and sensor. Since the alignment of the magnetic moments inside the paramagnetic sensor material along the external magnetic field depends on temperature, the temperature increase ΔT results in a reduction

$$\Delta M = \frac{\partial M}{\partial T}\Delta T = \frac{\partial M}{\partial T}\frac{\Delta E}{C_{\text{tot}}} \tag{2.2}$$

of the sensor magnetization M. This ΔM results in a flux change $\Delta\Phi$ inside a detection coil which is inductively coupled to a dc-SQUID:

$$\Delta\Phi \propto \Delta M \propto \Delta T \propto \Delta E\,. \tag{2.3}$$

In order to maximize the MMC signal, and therefore the signal to noise ratio, two requirements have to be fulfilled according to equations 2.2 and 2.3: Firstly, the heat capacity C_{tot} of sensor and absorber needs to be kept small. This is achieved by keeping both the absorber and sensor small in scale and operating the MMC at cryogenic temperatures below 100 mK inside a ^{3}He/^{4}He-dilution refrigerator, since the heat capacity of metals vanishes with decreasing temperature according to

$$C = C_{el} + C_{ph} = \gamma T + \beta T^3 \tag{2.4}$$

where γ and β are material dependent constants. The second requirement is a high temperature dependence $\partial M/\partial T$ of the sensor magnetization around the detector's operating temperature. Thus the choice of the right sensor material is of great importance and is discussed in the following section.

2.2 Sensor material

The choice of the right sensor material is crucial when building an MMC. At temperatures below 100 mK the coupling between phonons and magnetic moments of

dielectric materials is very weak, resulting in typical spin-phonon-relaxation times of seconds and more [Ban93]. To achieve faster thermalization times, it is beneficial to use paramagnetic ions which are embedded into a metallic host material. The ion spins can then thermalize by interacting with the conduction electrons of the metal, resulting in possible relaxation times below 100 ns [Fle09]. However a strong coupling between electronic and ionic spins also increases the heat capacity of the sensor and decreases the temperature dependence of its magnetization due to the RKKY[1]-interaction [Rud54, Kas56, Yos57]. This decreases the detector sensitivity as described by equation 2.2, i.e. a compromise between fast thermalization times and large signal heights has to be found. A good candidate for such paramagnetic ions are rear earth ions, since they interact comparably weakly with the conduction electrons of the host material. For the detector described in this thesis, erbium embedded in silver, henceforth called Ag:Er will be used. A detailed discussion of this material can be found in [Her21]. Such a material, silver doped with about 400 ppm erbium, was already used in [Sch21] and [Hen17] as a sensor material for other MMC-based detectors. Each erbium ion of the alloy sits on a regular lattice side inside the face centered cubic crystal structure of the silver, as shown in figure 2.2. It donates

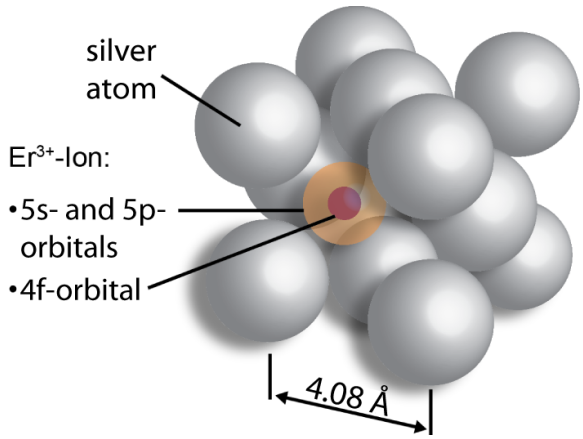

Figure 2.2: Schematic view of an atomic lattice section of the Ag:Er-alloy. It shows the silver atoms in fcc-structure and the 4f, 5s and 5p orbitals of an Er^{3+} ion substituting an atom of the host material on a regular lattice site.

three electrons to the system of delocalized conduction electrons of the metal. The resulting electron configuration of the Er^{3+} ions is $[Kr]4d^{10}4f^{11}5s^25p^6$. The radius of the incompletely filled $4f$-orbital is 0.3 Å [Fra76] which is small compared to the size of the entire ion. Due to the shielding by the outer $5s$ and $5p$ shells, the influence of the crystal field on the $4f$-orbital can therefore be neglected at temperatures above 100 K [Wil69]. In this approximation Hund's rules apply, resulting in a total electron spin $S = 3/2$, an orbital angular momentum $L = 6$ and a total angular momentum $J = L+S = 15/2$. From this the magnetic moment of the Er^{3+} ion can be calculated as

$$\mu = -\mu_B g_J J \tag{2.5}$$

[1]Ruderman-Kittel-Kasuya-Yosida

with Bohr's magneton $\mu_B = 9.27 \cdot 10^{-24}\,\mathrm{J/T}$ and a Landé-factor of

$$g_J = 1 + \frac{S(S+1) + J(J+1) - L(L+1)}{2J(J+1)} = \frac{6}{5}\,. \tag{2.6}$$

Still, at temperatures below 100 K the influence of the crystal field can no longer be neglected. Consequently, the $2J+1 = 16$ -fold degenerated ground state of the Er^{3+} ion is split into a series of multiplet states. The energy splitting between the resulting ground state doublet and the first excited multiplet corresponds to a temperature of 25 K as measured by [Hah92]. The temperature range interesting for this thesis lies far below that. As a result, the ion can here be approximated as a two-level system of the two ground states, with an effective spin $\tilde{S} = 1/2$ and an effective Landé-factor of $\tilde{g} = 6.84$ [Tao71].

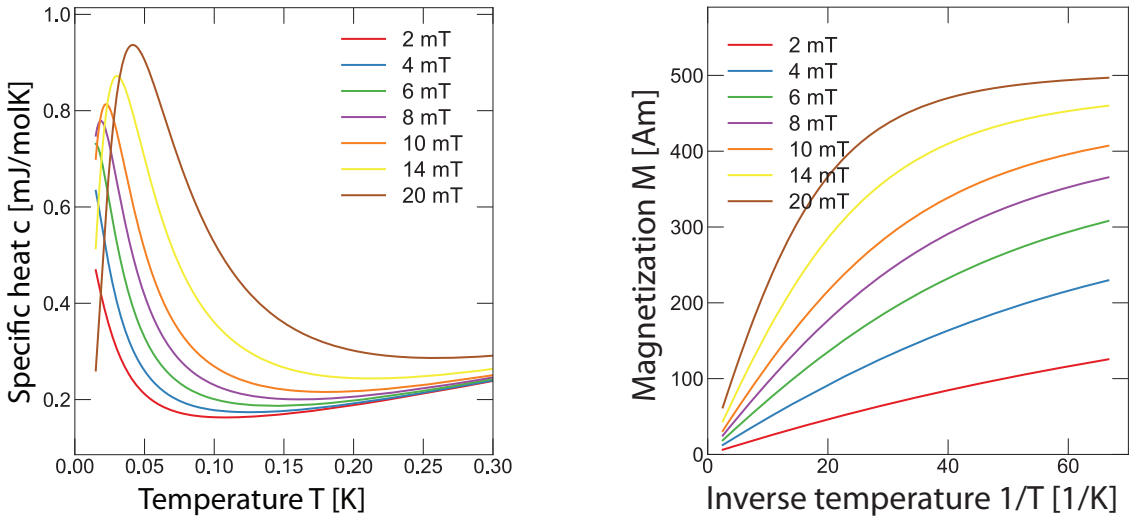

Figure 2.3: Simulated temperature dependency of the specific heat and the magnetization of an Ag:Er crystal for different magnetic fields, assuming an erbium concentration of 300ppm. The simulation was created by [Her21], based on [Sch00, Fle03, Fle05].

To understand the behavior of an MMC, the heat capacity C_s of the sensor and its magnetization change with temperature $\partial M/\partial T$ need to be known.
The electronic and phononic heat capacity of the sensor's metallic host material can be calculated according to equation 2.4. The additional spin contribution of the paramagnetic ions to the specific heat and the magnetization can qualitatively be approximated as the Zeeman splitting of an ensemble of non-interacting magnetic moments inside an external magnetic field. However, for quantitative estimates, a deeper treatment is necessary, where direct dipole-dipole interactions and the indirect

RKKY interactions between ions via polarization of the conduction electrons are considered. Figure 2.3 shows the simulated temperature dependency of the specific heat and the magnetization of an Ag:Er sample under consideration of both those interactions at different external magnetic fields. The simulations were created using a code by [Her21] based on [Sch00, Fle03, Fle05] and assume an erbium concentration of 300 ppm. The specific heat shows a Schottky anomaly with a maximum that increases with the external magnetic field, as does the temperature at which the sensor magnetization saturates.
If no isotopically pure erbium is used in the sensor material, the natural abundance of 22.9% ^{167}Er with nuclear spin $I = 7/2$ can lead to an additional reduction of the signal [Fle00]. Therefore, enriched erbium will be used for this detector.

2.3 Sensor readout

In an external magnetic field, the temperature change of the MMC resulting from the absorption of a particle leads to a decrease in sensor magnetization. This section explains how this magnetization change is measured with a coil that simultaneously provides the necessary magnetic field. It discusses the geometry of the detection coil itself, as well as the transformation of the magnetization change into a measurable voltage signal by a dc-SQUID.

2.3.1 Meander-shaped detection coils

In order to establish a good magnetic coupling between the sensor of an MMC and its detection coil (see figure 2.1), various possibilities are conceivable. In this thesis planar meander-shaped coils below planar sensors are used, since they allow a structuring of the detector in layers on a silicon wafer (see chapter 3). The coils consist of connected, parallel adjacent tracks, parameterized by a track width w and a center-to-center distance p (pitch), as depicted in figure 2.4.

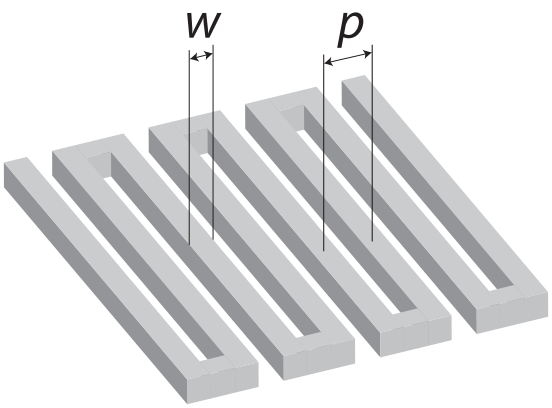

Figure 2.4: Schematic view of a planar meander-shaped detection coil, characterized by width w and pitch p. Figure taken from [Sch15].

The inductance L_m of a meander-shaped coil can be calculated as

$$L_\mathrm{m} = l\mu_0 \frac{A}{p}\,. \tag{2.7}$$

Here A is the area covered by the coil and $\mu_0 \approx 1.257 \cdot 10^{-6}\,\mathrm{Vs/Am}$ the vacuum permeability. The dimensionless geometry factor l depends on the ratio w/p and approximates to $l \approx 0.2$ for the parameters of $w = 4.5\,\mu\mathrm{m}$ and $p = 9\,\mu\mathrm{m}$ chosen in this thesis.

2.3.2 Generation of the magnetic field

The paramagnetic sensor of an MMC has to be magnetized inside an external magnetic field $\mathbf{B}$, as discussed in section 2.1. For the detector described in this thesis, a persistent super current I_0 is prepared inside the detection coil for this purpose. The resulting magnetic field is highly inhomogeneous, for instance as the direction of the magnetic field inverts after each distance p. Its spatial dependency can be put into a dimensionless, space dependent geometry factor

$$G(\mathbf{r}/p) = \frac{p}{\mu_0} \frac{\mid \mathbf{B}(\mathbf{r}) \mid}{I_0}\,. \tag{2.8}$$

2.3.3 Flux change in the detection coil

A change in the sensor magnetization ΔM results in a change $\Delta\Phi$ of the magnetic flux inside the detection coil, as discussed in section 2.1. This flux change can be calculated by first considering the infinitesimal flux change

$$\mathrm{d}(\Delta\Phi) = \mu_0 \frac{G(\mathbf{r}/p)}{p} \Delta M(\mathbf{r}) \mathrm{d}V \tag{2.9}$$

inside the coil, caused by an infinitesimal volume element $\mathrm{d}V$ of the sensor at position $\mathbf{r}$. The total flux change is obtained by integrating over the whole sensor volume V_s, using equation 2.2 as

$$\Delta\Phi = \frac{\Delta E}{C_\mathrm{a} + C_\mathrm{s}} \int_{V_\mathrm{s}} \mu_0 \frac{G(\mathbf{r}/p)}{p} \frac{\partial M(B(\mathbf{r}, T))}{\partial T} \mathrm{d}V\,. \tag{2.10}$$

Since this integral cannot be solved analytically due to the complicated spacial dependencies of B, the weighted average can be used instead, giving the expression

$$\Delta\Phi = \frac{V_\mathrm{s}}{C_\mathrm{a} + C_\mathrm{s}} \left\langle \mu_0 \frac{G(\mathbf{r}/p)}{p} \frac{\partial M(B(\mathbf{r}, T))}{\partial T} \right\rangle \Delta E \tag{2.11}$$

for the flux change inside the detection coil.

2.3.4 dc-SQUID

To measure the flux change calculated in the last section, a very sensitive magnetometer is necessary. The most precise method to measure magnetic fields is the use a superconducting quantum interference device (SQUID). The schematic structure of a dc-SQUID is sketched in figure 2.5 a). It consists of a superconducting loop,

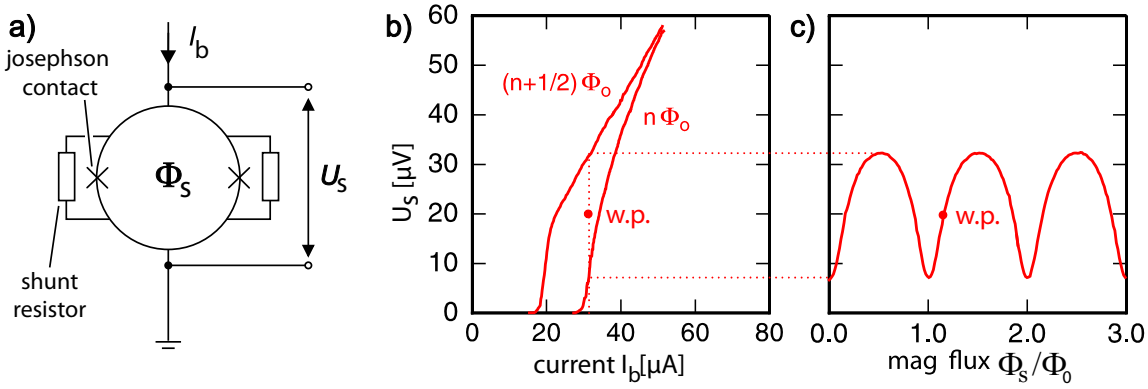

Figure 2.5: a) Circuit diagram of a dc-SQUID consisting of a superconducting loop, interrupted by two Josephson junctions, each with a shunt resistor added in parallel. b) Current-voltage characteristic of a dc-SQUID for magnetic fluxes $n\Phi_0$ and $(n + 1/2)\Phi_0$ inside the SQUID-loop. c) Dependency of the the voltage drop U_s across the SQUID on the trapped magnetic flux in units of Φ_0. Figure modified from [Gam19].

interrupted by two Josephson junctions, indicated by crosses. A Josephson junction is a weak link inside a superconducting circuit, typically realized as a thin layer of normal conducting material between two superconducting contacts. If a direct current I_b is driven through the SQUID, each junction can only carry a super-current up to a critical current $I_c/2$. Above this value, the current is carried by quasi particles, resulting in a finite voltage drop U_s over the SQUID, as depicted in 2.5 b). Generally, the magnetic flux Φ_s inside a closed superconducting loop is conserved and quantized as integer multiples of the flux quantum

$$\Phi_0 = h/2e = 2.07 \cdot 10^{-15}\,\mathrm{Vs}\,, \tag{2.12}$$

with Planck's constant h and elementary charge e. However, with the voltage drop, the SQUID loop is not completely closed and flux can leave or enter through the junctions. Since integer values of Φ_0 still minimize energy, any deviating flux is compensated by a screening current which adds to I_b in one junctions and subtracts from it in the other. The result is a periodic dependence of U_s on Φ_s as shown in figure 2.5 c). Therefore, the critical current I_c depends on the magnetic flux Φ_s inside

the SQUID loop and is maximized for integer multiples of Φ_0, as shown in figure 2.5 b) and c). If I_b is set at a value indicated as working point (w.p.) in figure 2.5 b) and c), even flux changes much smaller than Φ_0 result in a measurable voltage drop. To measure flux changes uniquely over a wide range, the flux-locked-loop setup described below is used.

2.3.5 Flux-locked-loop circuit

Single-stage flux-locked loop

The flux-voltage characteristic of a dc-SQUID depicted in figure 2.5 c) is periodic with periodicity Φ_0. Consequently, the SQUID can only function as a flux-to-voltage-converter over a small range of $\Phi_0/4$ without loosing uniqueness. In addition, the sensitivity (i.e. the slope of the curve) becomes very small for $\Phi_s = n\Phi_0$ or $\Phi_s = (n+1/2)\Phi_0$. To circumvent both of those problems, a flux-locked-loop can be deployed to operate the SQUID at its highest sensitivity over a large flux range. Such a circuit is schematically sketched in figure 2.6. It feeds the voltage drop U_s over the

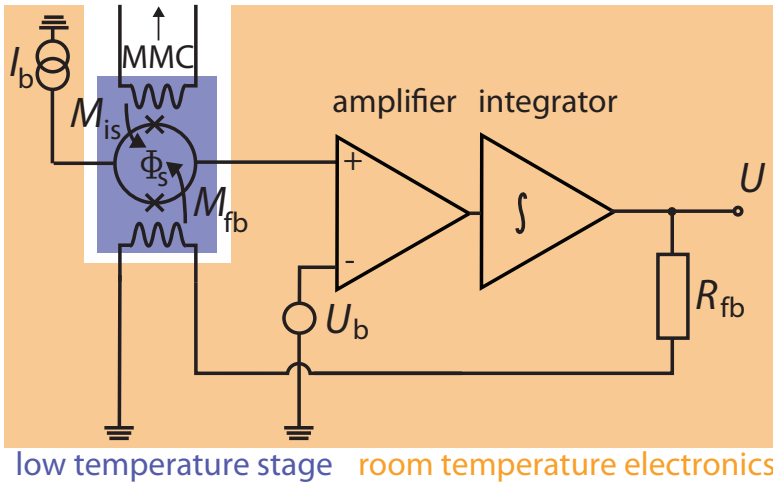

Figure 2.6: Flux-locked-loop circuit diagram used to linearize the output signal of a dc-SQUID. The electronics operated at low temperature and room temperature are indicated by different background colors.

SQUID into a differential amplifier at room temperature. The reference voltage for the amplifier is chosen as the voltage U_b at the SQUID working point, indicated in figure 2.5 c). The output of the amplifier is integrated by a voltage integrator which is connected to a feedback coil, in series with a feedback resistor R_{fb}. If the flux inside the SQUID changes, the voltage U_s shifts away from U_b, resulting in an output voltage U, leading to a current $I_{fb} = U/R_{fb}$ through the feedback coil. Mediated by the mutual inductance M_{fb}, the flux $\Phi_{fb} = M_{fb}I_{fb}$ is coupled into the

SQUID loop, compensating the initial flux change $\Delta\Phi_s$:

$$\Delta\Phi_s = -\Phi_{fb} = -M_{fb}\frac{U}{R_{fb}} \tag{2.13}$$

Therefore, the output voltage U corresponds to a linearized signal of the SQUID, proportional to the flux change $\Delta\Phi_s$.

Two-stage flux-locked loop

A weak point of the single-stage flux-locked loop is the fact that the output impedance of the of the SQUID at the low temperature stage is much lower than the input impedance of the amplifier at room temperature. Thus, to match the impedance of the two stages and therefore improve the overall noise behavior, the SQUID signal can be amplified inside the cryostat at low temperatures. For this purpose, a so called two-stage flux-locked loop circuit is used which is shown schematically in Figure 2.7. To pre-amplify the detector signal, 16 additional SQUIDs which are

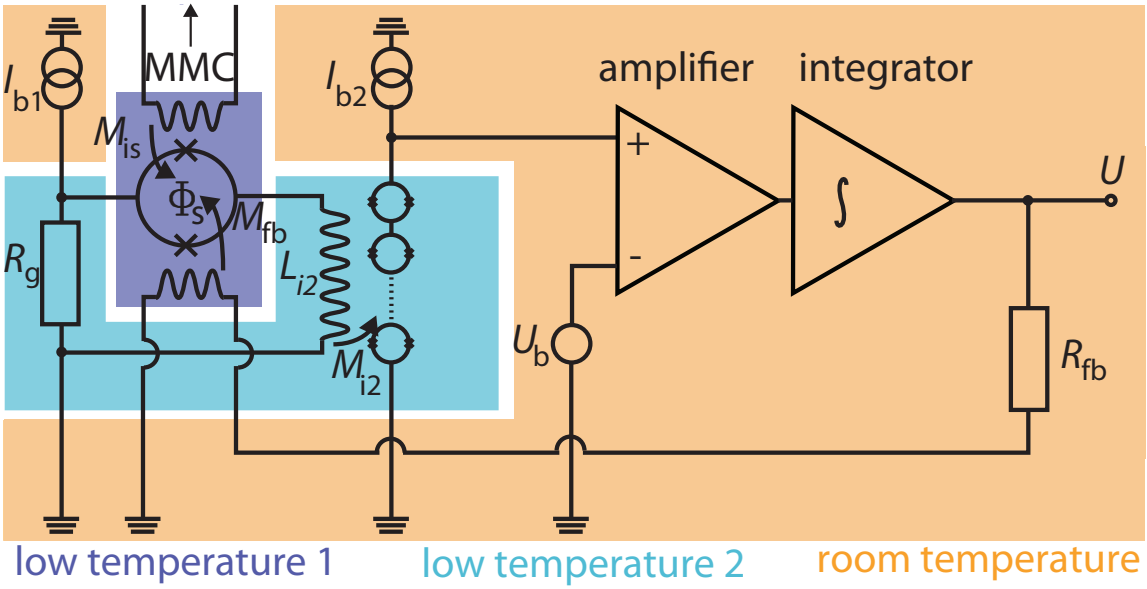

Figure 2.7: Two-stage flux-locked loop circuit diagram used linearize and to amplify the output signal of detector dc-SQUID (at low temperature 1) with SQUID array (at low temperature 2). Electronics operated at low temperature region 1, 2 and room temperature are indicated by different background colors.

connected in series can be used that couple to a common input coil L_{i2}. The 16 SQUIDs therefore share a common bias current I_{b2}. Such a SQUID-array behaves in good approximation as a single SQUID with a 16-times larger output voltage. The

detector SQUID coupled to the MMC is connected in parallel with a gain resistor R_g and in series with the common input coil L_i2 of the SQUID array. This input coil couples to the SQUID array with a mutual inductance M_i2. The bias current I_b1 of the original SQUID splits and flows in part through the gain resistor R_g and in part through the SQUID with the inductance L_i2 connected in series. Hence, the working point of the detector SQUID is dependent on both I_b1 and the gain resistor R_b. If the latter is chosen to be much smaller than the impedance of the detector SQUID, the voltage-drop across the SQUID will remain approximately constant. This enables the operation of the detector SQUID as a flux-to-current converter. A flux change in the detector SQUID therefore leads to a current change inside the input coil L_i2 which couples into the SQUID-array. The SQUID array is connected to the room temperature electronics which are similar to the single-stage flux-locked loop. The output voltage U of the integrator drives a current through the feedback coil of the detector SQUID via a feedback resistor R_fb. This again couples the signal into the detector SQUID with the mutual conductance M_fb and therefore keeps it at the working point over a wide range of magnetic flux. Thus, the circuit again functions as a linear flux-to-voltage-converter, since

$$U = \frac{R_\mathrm{fb}}{M_\mathrm{fb}} \Delta\Phi_\mathrm{s} = \frac{M_\mathrm{is}}{M_\mathrm{fb}} I_\mathrm{s} \,. \tag{2.14}$$

2.3.6 Flux change inside the SQUID

As stated before, the magnetic flux Φ inside of a closed superconducting loop is quantized to integer multiples of the magnetic flux quantum Φ_0 (see equation 2.12). Therefore, if an MMC is operated at cryogenic temperatures with a superconducting detection coil and if a change in sensor magnetization leads to a flux change $\Delta\Phi < \Phi_0$ in the coil, a screening current ΔI_s is induced inside the superconducting network, raising or lowering the trapped flux to the nearest integer multiple of Φ_0. If two identical detection coils are gradiometrically connected to the SQUID input coil as depicted in figure 2.8, ΔI_s can be calculated using Kirchhoff's laws as

$$\Delta I_\mathrm{s} = \frac{\Delta\Phi_1 - \Delta\Phi_2}{L_\mathrm{m} + 2(L_\mathrm{i} + L_\mathrm{b})} \,. \tag{2.15}$$

Here, $\Delta\Phi_1$ and $\Delta\Phi_2$ are the flux changes in the two detection coils, L_m is given by equation 2.7 and L_i is the inductance of the SQUID input coil. Since the latter is part of a separate SQUID chip that is connected to the detection coils via thin aluminium wires, the additional inductance L_b of the bonding wires must be taken into account here. This geometry is advantageous, since external magnetic field changes or changes in sensor temperature which are identical for both coils neutralize each other.

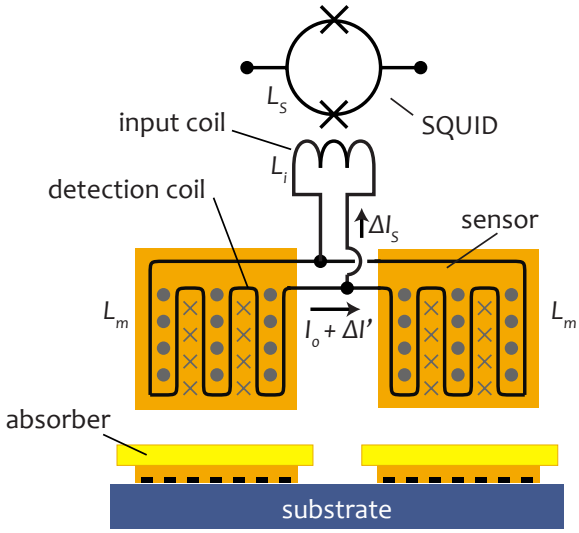

Figure 2.8: Schematic view of a flux transformer circuit with two gradiometrically wired meander-shaped detection coils for the simultaneous readout of two sensors with one SQUID. Figure modified from [Sch21].

The current change ΔI_s inside the input coil corresponds to a flux change

$$\Delta\Phi_\mathrm{s} = M_\mathrm{is}\Delta I_\mathrm{s} \tag{2.16}$$

inside the SQUID with inductance L_s, where the mutual inductance is calculated from the coupling factor k as

$$M_\mathrm{is} = k\sqrt{L_\mathrm{i}L_\mathrm{s}}\,. \tag{2.17}$$

Combining the last three equations, the flux change inside the SQUID is given as

$$\Delta\Phi_\mathrm{s} = \frac{k\sqrt{L_\mathrm{i}L_\mathrm{s}}}{L_\mathrm{m} + 2(L_\mathrm{i} + L_\mathrm{b})}(\Delta\Phi_1 - \Delta\Phi_2)\,. \tag{2.18}$$

2.4 Signal shape

Having summarized the operation of MMCs, the shape of the signals produced by the detection of particles is discussed in the following. They can be characterized by the maximum signal height, rise time, decay time and noise.

2.4.1 Signal height

As discussed in section 2.1, the signal height of an MMC is proportional to the change in sensor magnetization. The change of the magnetic moment caused by the whole sensor is calculated by integrating the change in magnetization at position $\mathbf{r}$ over its volume V_s. The potential energy E of the magnetic moment $\mathbf{m}$ in the external magnetic field $\mathbf{B}$ is given as

$$E = \mathbf{m}\cdot\mathbf{B}\,. \tag{2.19}$$

The combined heat capacity of one sensor and its absorber consists of the phononic contribution $C_{\mathrm{ph}}(T)$, the contribution of the conduction electrons $C_{\mathrm{e}}(T)$ and the field dependent Zeeman contribution $C_{\mathrm{Z}}(B,T)$ of the spins. Therefore, if a particle deposits an energy ΔE inside the sensor and absorber, only a fraction of this energy which is stored in the spin system, contributes to a change in magnetic moment, resulting in

$$\Delta m = \frac{C_{\mathrm{Z}}(B,T)}{C_{\mathrm{Z}}(B,T) + C_{\mathrm{e}}(T) + C_{\mathrm{ph}}(T)} \frac{\Delta E}{B}\,, \tag{2.20}$$

assuming thermal equilibrium between all three heat capacities.

2.4.2 Signal rise and decay time

The thermal properties of an MMC can be modeled as depicted in figure 2.9. The

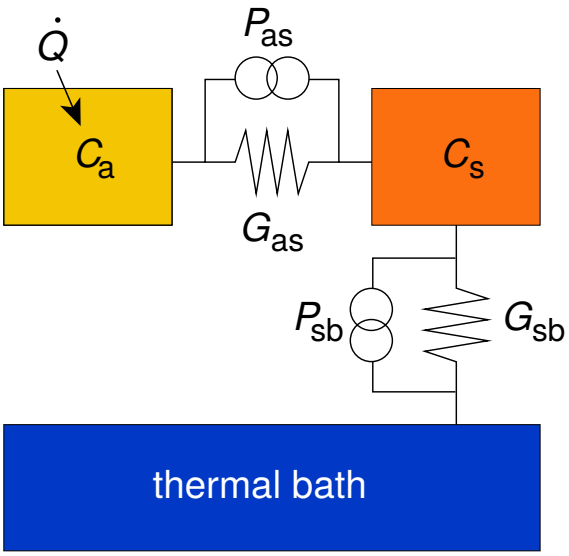

Figure 2.9: Thermal equivalent circuit diagram of an MMC. Depicted are the two subsystems of absorber and sensor with heat capacities C_{a} and C_{b} together with a thermal bath. The thermal connections G_{as} and G_{sb} are complemented with noise sources P_{as} and P_{sb}.

heat capacity C_{a} of the absorber is coupled via a thermal link G_{as} to the heat capacity C_{s} of the sensor. The sensor in turn is connected to a thermal bath at constant temperature T_0 via the link G_{sb}. Assuming an instantaneous energy input $\Delta E\delta(t)$ inside the absorber if a particle hits the detector and neglecting the noise sources P_{as} and P_{sb} for now, the system is described by the coupled differential equations

$$\dot{E}_{\mathrm{a}} = C_{\mathrm{a}}\dot{T}_{\mathrm{a}}(t) = -(T_{\mathrm{a}} - T_{\mathrm{s}})G_{\mathrm{as}} + \Delta E\delta(t) \tag{2.21}$$

$$\dot{E}_{\mathrm{s}} = C_{\mathrm{s}}\dot{T}_{\mathrm{s}}(t) = -(T_{\mathrm{s}} - T_{\mathrm{a}})G_{\mathrm{as}} - (T_{\mathrm{s}} - T_0)G_{\mathrm{sb}}\,. \tag{2.22}$$

Here $E_i = C_i T_i(t)$ denotes the thermal energy inside the subsystem of the absorber and the sensor respectively. For the detector discussed in this thesis, the thermal link between the thermal bath and the sensor is weak compared to the coupling between

absorber and sensor. Therefore, assuming $G_{\mathrm{as}} \gg G_{\mathrm{sb}}$, equations 2.21 and 2.22 are solved by

$$E_{\mathrm{s}}(t) = \Delta E p(t) \tag{2.23}$$

with the point spread function

$$p(t) \approx \frac{C_{\mathrm{s}}}{C_{\mathrm{tot}}}(-\exp(-t/\tau_a) + \exp(-t/\tau_b))\,. \tag{2.24}$$

In this approximation, the rise time is given as

$$\tau_a \approx \frac{C_{\mathrm{a}} C_{\mathrm{s}}}{C_{\mathrm{tot}} G_{\mathrm{as}}} \tag{2.25}$$

while the decay time is calculated as

$$\tau_b \approx \frac{C_{\mathrm{tot}}}{G_{\mathrm{sb}}}\,. \tag{2.26}$$

Both time constants are approximately temperature independent and can be adjusted by the detector design. How this fact can be exploited in the case of τ_b for the readout of many sensors with only a few SQUIDs is discussed in chapter 3.

2.4.3 Fundamental energy resolution

When discussing the energy resolution of an MMC, the thermal model shown in figure 2.9 can again be considered. The noise contributions due to thermal fluctuations inside the thermal links are depicted as power sources P_{as} and P_{sb}. Their power spectra are frequency independent and can be described along the lines to the current noise of electrical resistors as

$$S_{P_{ij}} = 4 k_{\mathrm{B}} T^2 G_{ij}\,, \tag{2.27}$$

with the Boltzmann constant $k_{\mathrm{B}} = 1.38 \cdot 10^{-23}\,\mathrm{J/K}$ and the index $ij = as$ or sb. Assuming no particle hits ($\Delta E \delta(t) = 0$), equations 2.21 and 2.22 can be modified to include the noise sources P_{as} and P_{sb}. A Fourier transformation into frequency space then yields the expression

$$S_{E_s}(f) \approx 4 k_{\mathrm{B}} T^2 C_{\mathrm{s}} \left((1-\beta)\frac{\tau_a}{1+(2\pi\tau_a f)^2} + \beta \frac{\tau_b}{1+(2\pi\tau_b f)^2} \right)\,, \tag{2.28}$$

when assuming $\tau_a \ll \tau_b$ and values of $C_{\mathrm{a}} \approx C_{\mathrm{s}}$. Here $\beta \approx C_{\mathrm{s}}/C_{\mathrm{tot}}$ is the ratio between the heat capacities of the sensor and the whole MMC. From this, the signal-to-noise-ratio (SNR) can be calculated using the Fourier transform of the point spread function $\bar{p}(f)$ from equation 2.24 as

$$\mathrm{SNR}^2(f) = \frac{|\,\bar{p}(f)\,|^2}{S_{E_s}(f)} \approx \frac{1}{k_{\mathrm{B}} T^2 C_{\mathrm{s}}} \left(\frac{\beta \tau_b}{1 + \frac{1-\beta}{\beta}\tau_a \tau_b (2\pi f)^2} \right)\,. \tag{2.29}$$

From this, the instrumental line width

$$\begin{aligned}\Delta E_{\mathrm{FWHM}} &= 2\sqrt{2\ln 2}\left(\int_0^\infty \mathrm{SNR}^2(f)\mathrm{d}f\right)^{-1/2} \\ &\approx 2\sqrt{2\ln 2}\sqrt{4k_\mathrm{B}T^2C_\mathrm{a}}\left(\frac{1}{\beta(1-\beta)}\right)^{1/4}\left(\frac{\tau_a}{\tau_b}\right)^{1/4}\end{aligned} \tag{2.30}$$

can be calculated as shown in [Fle03]. It defines a fundamental limit of the energy resolution achievable with an MMC. The instrumental line width is minimized for $\beta = \frac{1}{2}$, meaning ideally the absorber and sensor heat capacities are equal. To further improve energy resolution, a fast rising signal with a long decay time is desirable. Assuming a metallic absorber with $C_\mathrm{a} \propto T$, equation 2.30 is proportional to $T^{3/2}$.

2.4.4 Additional noise contributions

In addition to the intrinsically limited energy resolution of the MMC, other noise sources must be taken into account which are briefly discussed in the following.

Magnetic Johnson Noise

In an electrical conductor at equilibrium, the thermal agitation of the conduction electrons generates electronic noise weather or not any voltage is applied. This electronic noise results in additional, so called magnetic Johnson noise S_{Φ_J} inside the detection coils. The main contributor to this are normal conducting detector components like the absorbers, sensors and other pieces made from non superconducting metals. Magnetic Johnson noise is approximately white, meaning the spectral density is independent of frequency. It becomes smaller with decreasing temperature and becomes typically negligibly small compared to other noise contributions for detectors using paramagnetic metallic sensors [Pie12].

Erbium 1/f noise

In MMCs with Ag:Er as sensor material, an additional noise contribution which is approximately inverse proportional to frequency was measured [Bur08]. This noise contribution is proportional to the concentration N_Er of the Er^{3+} ions inside the sensor material and does not depend on temperature between 30 mK and 4.2 K. As shown in [Fle09], a power density of

$$S_\mathrm{m}(f) \approx 0.1\frac{\mu_\mathrm{B}^2}{f^\nu} \tag{2.31}$$

can typically be attributed to every Er^{3+} ion inside the sensor. Here, the exponent ν is a geometry dependent constant between 0.8 and 1. By integrating over all ions, the resulting total noise inside a meander shaped detection coil with pitch p can be calculated as

$$S_{\Phi_{\mathrm{Er}}}(f) = \frac{\mu_0 \langle G^2 \rangle}{p^2} S_{\mathrm{m}}(f) N_{\mathrm{Er}} \propto \frac{N_{\mathrm{Er}}}{f^{\nu}}\,, \tag{2.32}$$

using the weighted geometry factor G from equation 2.2. The exact physical explanation for this effect is not yet known. Nevertheless, similar fluctuations of magnetic moments at far lower temperatures have been found in spin glasses by [Kog81].

2.4.5 SQUID-noise

The magnetic flux noise

$$S_{\Phi_{\mathrm{S}}} = S_{\Phi_{\mathrm{S,w}}} + S_{\Phi_{\mathrm{S,f}}} \tag{2.33}$$

intrinsic to dc-SQUIDs consists of a frequency independent white component $S_{\Phi_{\mathrm{S,w}}}$ and a frequency-dependent pink contribution $S_{\Phi_{\mathrm{S,f}}}$.

White noise

The white contribution to the SQUID noise originates from the thermal noise of the two shunt resistors R_{S}, connected in parallel to the two Josephson junctions (see figure 2.5). Using optimized SQUID parameters which were determined by numerical calculations in [Tes77] and [Bru82], the apparent flux noise measured by the SQUID can be expressed as

$$S_{\Phi_{\mathrm{S,w}}} \approx 18 k_{\mathrm{B}} T \frac{L_{\mathrm{S}}^2}{R_{\mathrm{S}}}\,. \tag{2.34}$$

Here L_{S} is the inductance of the SQUID loop. For typical values of the SQUID inductance and the shunt resistances of $L_{\mathrm{S}} \approx 100\,\mathrm{pH}$ and $R_{\mathrm{S}} \approx 5\,\Omega$ at 150 mK, a white SQUID-noise of $\sqrt{S_{\Phi_{\mathrm{S,w}}}} \approx 1.3 \cdot 10^{-7}\,\Phi_0/\sqrt{\mathrm{Hz}}$ is expected.

Pink noise

The noise dependent contribution $S_{\Phi_{\mathrm{S,f}}}$ often behaves according to

$$S_{\Phi_{\mathrm{S,f}}} \approx \frac{1}{f^{\alpha}} \tag{2.35}$$

with the exponent α taking values between 0.6 and 1.2 [Kem16]. It increases with decreasing temperature and tends to dominate the white contribution in the mK-range. The physical origin of this noise is partially unknown but there are theories tracing it back to the noise of magnetic moments on the surface of the SQUID loop [Koc07] or the vicinity of the two Josephson junctions [Kum16, DG17].

2.4.6 Total noise

All noise contributions discussed above are statistically independent of each other and can thus be summed up to obtain the total noise

$$S_{\Phi_{\mathrm{tot}}}(f) = \left(\frac{\Delta\Phi_{\mathrm{S}}}{\Delta\Phi}\right)^2 \left[S_{\Phi_{\mathrm{J}}} + S_{\Phi_{\mathrm{Er}}}(f) + S_{\Phi_{\mathrm{Es}}}(f)\right] + S_{\Phi_{\mathrm{S}}}(f) \tag{2.36}$$

inside the SQUID, where $\Delta\Phi_{\mathrm{S}}/\Delta\Phi$ is the flux-to-flux coupling between detection coil and SQUID.

2.5 Detection of massive particles with MMCs

When using MMCs to measure the kinetic energy of massive particles instead of their more common application as photon detectors, some additional effects need to be taken into account.
An incident massive particle hitting the absorber of an MMC looses its kinetic energy by scattering with the conduction electrons and the ion cores of the absorber material (see section 2.1), resulting in an increase of the absorber temperature. However, the following three mechanisms can lead to an energy loss which is not converted to heat and thus lost to the measurement:

- **Backscattering** : As depicted in figure 2.10 a), the incident particle can be scattered back after hitting the absorber material, taking some kinetic energy with it. Consequently, this energy is not measured as a temperature increase of the absorber.

- **Sputtering** : Atoms of the absorber can gain enough energy by scattering with the incident particle to leave the material, leading to their kinetic energy being lost to the measurement. This process, shown in figure 2.10 b), is called sputtering.

- **Frenkel defect formation** : The incident particle can scatter an atom from the absorber to an interstitial lattice site, leaving its regular lattice position vacant. This process, known as the formation of Frenkel defects, is depicted in figure 2.10 c). At room temperature, the resulting, energetically unfavorable state quickly relaxes into the original position. Still, at low temperatures below 100 mK, the Frenkel defect remains stable [DW75]. Since a massive particle with a kinetic energy of some 100 keV can create hundreds of Frenkel defects upon absorption, this can cause a significant degradation of energy resolution.

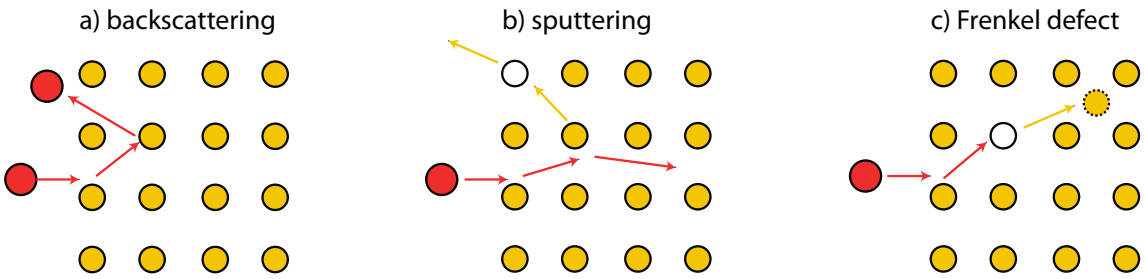

Figure 2.10: Schematic drawings of the possible effects when absorbing a massive particle in an absorber: a) backscattering of the incident particle, b) sputtering of absorber atoms and c) creation of a Frenkel lattice defect. The atoms of the absorber material are depicted in yellow, the incident particle red and empty lattice sites white. Figure modified from [Gam19].

In order to minimize these effects, the right choice of absorber material is important when building an MMC. Generally speaking it should be normal conducting and metallic, since dielectric or superconducting absorbers have shown to lead to additional long lived excitations that are not well understood. Simulations in [Gam17, Gam19] have shown aluminium to be a most suitable absorber material in terms of nucleus size, but the problem of superconductivity would have to be solved here. Possible solutions are thin aluminium films or suitable alloys.

2.6 Thermal conductivity at low temperatures

The signal decay time τ_b of an MMC which depends on the thermal connection G_{sb} between sensor and thermal bath (see figure 2.9 and equation 2.26) is of great importance for the detector featured in this thesis. Therefore, this section gives a brief description of the thermal conductivity of the different types of materials below 1 K. For a more involved explanation see e.g. [Hun17].

Metals

Metals that do not become superconducting below 100 mK like gold or silver are characterized by the presence of conduction electrons. These electrons dominate heat transport at low temperatures, with the thermal conductivity λ being connected to the electric conductivity σ by the Wiedemann-Franz Law

$$\frac{\lambda}{\sigma} = LT\,, \tag{2.37}$$

with the Lorenz number $L = 2.44 \cdot 10^{-8}\,\mathrm{W\Omega K^{-2}}$. At 300 K, the electric conductivity is determined by collisions of electrons with lattice defects and phonons. Since the

latter die out at temperatures below the material dependent Debye temperature $T \ll \Theta_\mathrm{D}$, the conductivity σ at low temperatures is dominated by defect scattering. For bulk materials the residual resistance ratio

$$RRR = \frac{\sigma(4.2\,\mathrm{K})}{\sigma(300\,\mathrm{K})} \tag{2.38}$$

is often measured, connecting the electric conductivities at room temperature and at the boiling point of helium. At temperatures below 4.2 K, the mean free path of conduction electrons in most metals is limited by defects and therefore constant. Accordingly, the conductivity for temperatures $T < 4.2\,\mathrm{K}$ can also be calculated from equation 2.38.

Non-metallic solids

The absence of conduction electrons in dielectric solids like SiO_2 leaves the heat transport to phonons. The resulting expression for the thermal conductivity follows from the theory of ideal gases as

$$\lambda = \frac{1}{3} C_\mathrm{ph} v_\mathrm{D} l \tag{2.39}$$

with C_ph from equation 2.4, the speed of sound v_D and the mean free path l. At low temperatures, l is limited by lattice defects, including the geometric dimensions of the material, and therefore constant. The resulting behavior $\lambda \propto T^3$ means that the thermal conductivity of dielectrics is usually much smaller than that of metals at low temperatures. Furthermore, at boundaries between two materials of differing acoustic impedance, phonons can be reflected, leading to additional Kapitza-resistances (e.g. [Ens00] for further detail).
The behavior of semi- and superconductors like silicon or niobium is similar to dielectric materials, since there are no thermally excited charge carriers in semiconductors at low temperatures, while almost all conduction electrons in a superconductor are condensed into a common BCS-ground state ([Hun17] for further detail), making entropy transport impossible.

3. Detector design

As stated in the introduction, the scope of this thesis is the development of a detector for the energetically and spatially resolved detection of neutral molecule fragments which are formed in dissociative recombination reactions at the cryogenic storage ring CSR of the Max-Planck-Institute for Nuclear Physics in Heidelberg. The measured kinetic energy could then be used to determine the mass of the products, whereas the spatial resolution together with the time of detection would give the energy released during the reaction. A detector suitable for this purpose needs to fulfill the following requirements:

- A high quantum efficiency for the detection of neutral molecule fragments with kinetic energies up to 300 keV
- A high energy resolution $\Delta E < 1\,\mathrm{keV}$
- Fast signal rise times $\tau_a < 1\,\mu\mathrm{s}$ to ensure a high time resolution
- Operation in a cryogenic environment below 10 K
- A highly resolved position sensitivity over a large detection area with a diameter between 4 cm and 10 cm

A viable base for such a detector are MMCs which were discussed in chapter 2, since they inherently meet all of the above criteria - except for position sensitivity. To combine these beneficial properties with a high spatial resolution, the detector design presented in this thesis features a 4.48 cm × 4.48 cm pixel array, consisting of 64 × 64 separate MMCs.

This chapter discusses the detector design, starting with the newly developed readout scheme. In the following, the signal decay time τ_b of an MMC (see 2.26) is referred to as τ for simplicity reasons.

3.1 Readout scheme

The high spatial and energetical resolution is realized by a 4.48 cm × 4.48 cm detection area filled with 700 μm × 700 μm MMC based pixels. A simultaneous readout of the resulting 64 × 64 pixel array with one SQUID per pixel would not be feasible, since the voltage drop U_s over each SQUID would result in a Joule heating of

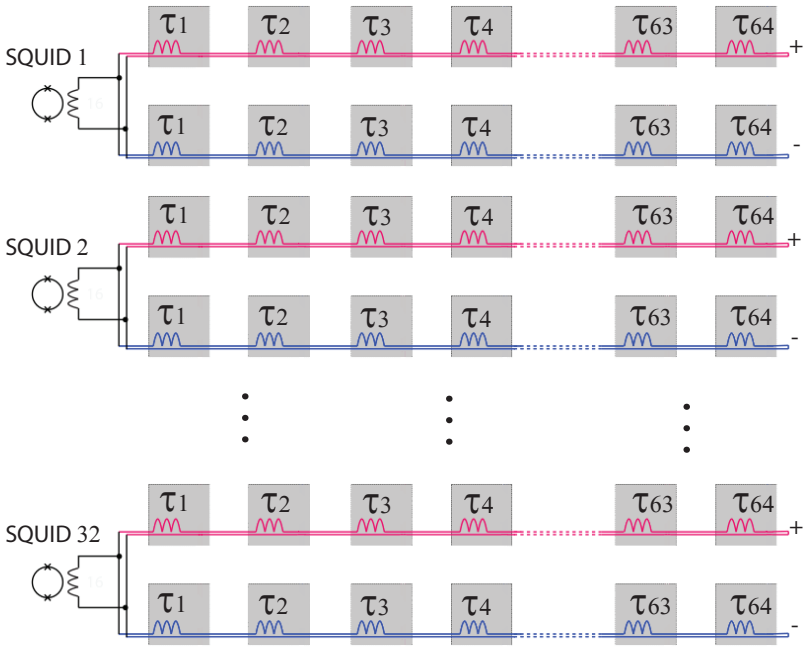

Figure 3.1: Schematic representation of the readout scheme developed in this thesis for a simultaneous readout of 64 × 64 MMC pixels with 32 SQUIDs. The assignment of the rows is given by the SQUID number and the polarity of the row (shown in red and blue). The differentiation between the columns is achieved by 64 different signal decay times τ_i.

$P = U_s I_b$ per SQUID (see section 2.3.4). This heating power makes the operation of thousands of SQUIDs at temperatures below 100 mK inside a conventional dilution cryostat problematic. Furthermore, the cost and complexity of the electronics required to operate such a large number of SQUIDs would be enormous and may result in further heating. Therefore, a new readout scheme was developed in this thesis, enabling the readout of the 4096 pixels with only 32 SQUIDs. Figure 3.1 shows a sketch of the 64 × 64 MMCs (as gray squares) and their connections to the SQUIDs via the detection coils and the SQUID input coils, as discussed in chapter 2.3.6. Instead of a separate detection coil for each MMC, the coils belonging to a row of 64 pixels are connected in series, forming one large common detection coil for the entire row. Each SQUID couples to two neighboring pixel rows which are connected to the SQUID's input coils with different polarities, shown in red and blue. If a particle hits an absorber, a change in magnetic flux is detected by one of the 32 SQUIDs as discussed in section 2.1. Depending on the polarity of the signal, the row in which the hit occurred is uniquely determined.
The information in which column the hit occurred is encoded into the decay time of the pulse. The MMC pixels of column i each share the same decay time τ_i, with decay times differing slightly but sufficiently between columns, so that a clear assignment of the signals to the columns is possible. As discussed in section 2.4, the decay

time of an MMC is calculated as $\tau \approx C_{\mathrm{tot}}/G_{\mathrm{sb}}$ in good approximation. The variation of τ should not be reached via the heat capacity C_{tot} of absorbers and sensors, because otherwise each of the 64 pixels would need a different geometry and would therefore behave drastically different. Thus, the only reasonable implementation of the readout scheme is to vary the thermal couplings G_i between the i-th sensors and the thermal bath, as depicted in figure 3.2.

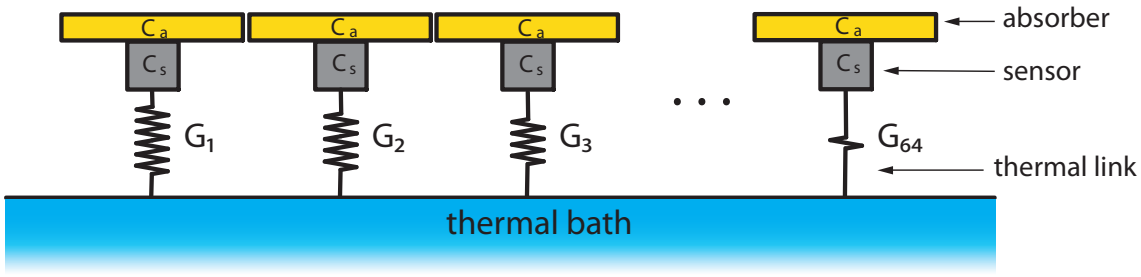

Figure 3.2: Schematic view of the 64 different thermal links connecting the sensors of one row to the thermal bath, resulting in 64 different signal decay times.

Together, the two mechanisms of identifying detected pulses with the rows and columns enable the full spatial resolution of the detector with only 32 SQUIDs. However, this substantial reduction in readout complexity comes at a price:

The first consequence is an increase in the error sensitivity of the detector. In contrast to autonomously operating MMCs, errors in individual pixels may effect two hole rows of 64 MMCs each. This poses special requirements for the design of the MMCs detection coils which are discussed in section 3.3.

Secondly, the readout scheme restricts the maximum measurement frequency. The limiting parameter for the time between the detection of two particles at full energy resolution by an MMC is the signal decay time τ (see equation 2.26). This would not be a problem for a pixel array where every MMC pixel functions completely autonomously, since the probability for two particles hitting in short succession onto the same pixel would be low. With this newly proposed readout scheme on the other hand, two particle hits in short succession somewhere inside the two pixel rows connected to the same SQUID are already sufficient to interfere with each other. This problem is worsened by the fact that the decay times of some MMCs inside these rows have to be artificially long, in order to reliably distinguish between columns. Therefore, a compromise between long decay times for an easy column discrimination and a high intrinsic energy resolution (see equation 2.30) on the one hand and short

decay times for a high measurement frequency of the detector on the other hand needs to be found. The compromise realized in this design is discussed in section 3.4.1.

Finally, the independent noise contributions originating from each MMC, are now all coupled into the SQUID they are connected to. As a result, each SQUID measures a noise contribution coming from the MMCs that is at least a factor of $\sqrt{64+64}$ larger than that of a single pixel (resulting from the two rows of 64 MMCs connected to the SQUID). Therefore, the expected energy resolution of the detector is much worse than the fundamental limit calculated in equation 2.30. The expected energy resolution is discussed in section 3.9.

3.2 General detector structure

The detector will be fabricated on a three-inch silicon wafer which is cut into a $5.48\,\text{cm} \times 5.48\,\text{cm}$ chip, as depicted in figure 3.3. This illustration and all subsequent drawings of the detector design are excerpts from the design drawings made in the framework of this thesis in Cadence Virtuoso Layout[1]. The following descriptions of the design often refer to "left", "right", "up" and "down". These specifications always refer to the orientation of the chip chosen in figure 3.3 which stays the same in all illustrations. The detector features 64 rows of 64 MMC pixels each over a square detection area with an edge length of 4.48 cm. The enlargement shows an MMC circled in pink which consist of a square absorber (yellow) coupled to a square sensor (blue). The absorbers fill 99.4% of the detection area. To make the underlying structures visible, of which none can be seen on the actual chip, the absorbers are depicted in transparent yellow. The properties of the absorbers are discussed in detail in section 3.11.

The detection coils belonging to the MMCs in a row are connected in series to form one large common coil for the entire row. The resulting coils of two adjacent rows are connected to a bond pad on the left. These pads will later be connected to the input coils of the 32 readout SQUIDs via thin aluminum wires. Both the input coils and the SQUIDs are located on separate chips and not depicted. On the right, the detection coils are connected by a circuit enabling the preparation of persistent supercurrents which features additional bond pads for two current sources in the top right corner. The enlargement in figure 3.3 shows one such current switch on the right side. All the current carrying structures are discussed in detail in the following section 3.3.

[1] Cadence Design Systems, San José, California, USA

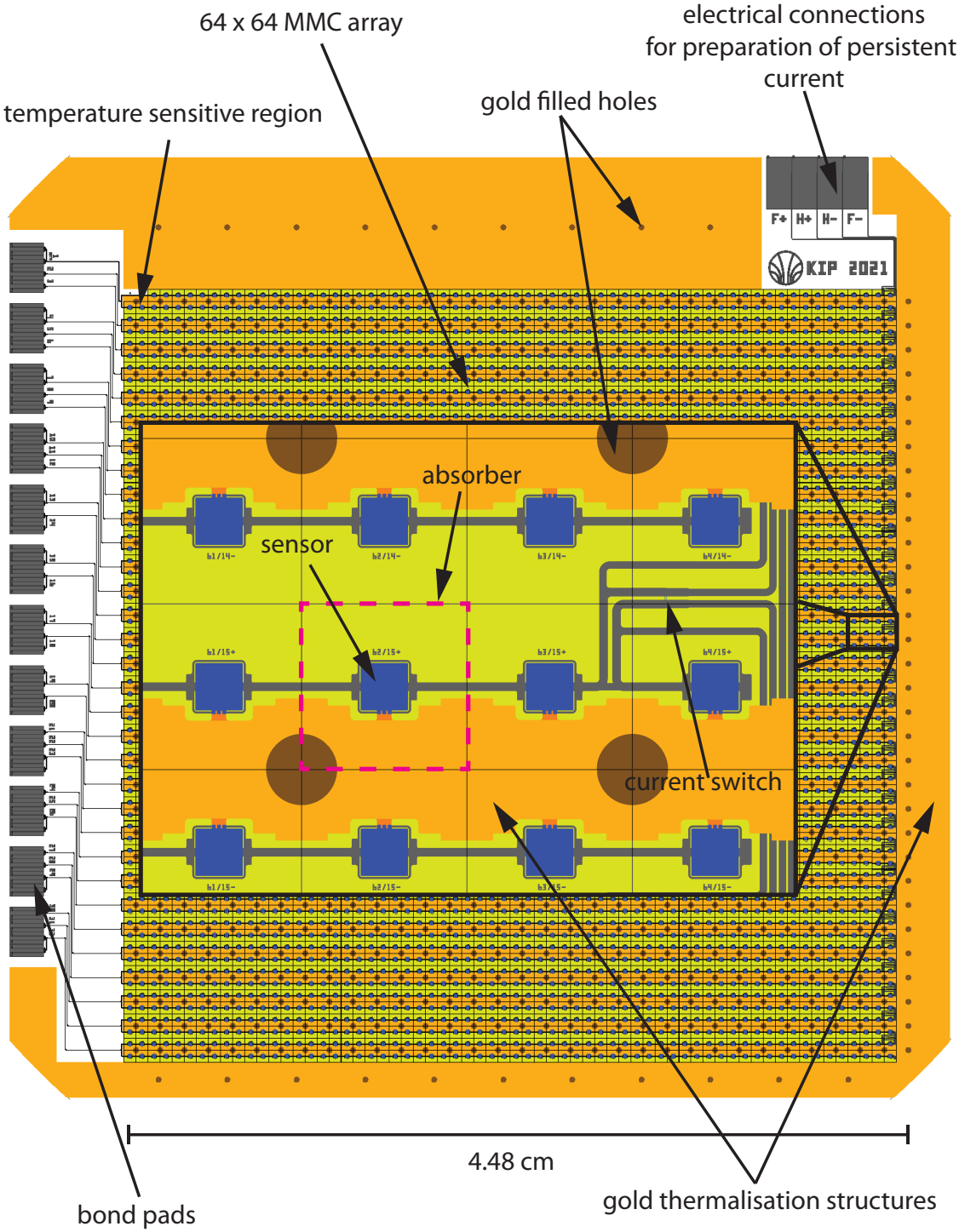

Figure 3.3: Detector design, consisting of 64 × 64 MMCs. The absorbers are depicted in transparent yellow, for a better view of the underlying structures. They are discussed in section 3.5. The current carrying structures (coils, bond pads and current switches; all depicted in gray) are discussed in section 3.3. The sensors (depicted in blue) and the golden thermalization structures (depicted in orange), including the optional gold filled holes through the wafer (depicted in brown) are discussed in section 3.4. The temperature sensitive region refers to the optional temperature pixels which are discussed in section 3.6.

Gold surfaces are patterned between the rows and around the detection area, depicted in orange. They form thermal connections between the MMC sensors and a thermal bath which is a massive copper holder beneath the chip (not depicted). To this end, the right, upper and lower edges of the chip can be connected to the copper holder by gold wires. Additionally, the gold structures can be connected to the copper holder via gold filled holes through the wafer, depicted in brown. The gold structures are designed to vary the thermal connection of each sensor which allows spatial information to be encoded into the signal decay times, as discussed in section 3.1. The gold structures, their thermal properties and the exact implementation of the readout scheme are discussed in detail in section 3.4.

The detector features an optional temperature sensitive region in the top left corner of the detection area. How it can be used as a thermometer is discussed in section 3.6.

All structures in the design, with the exception of the absorbers, have rounded corners as this limits the possibility of locally large electric fields and may facilitate fabrication. The materials and thicknesses of all the detector components are summarized in section 3.7, after the discussion of the schematic detector layout.

3.3 Current carrying structures

The current-carrying structures of the detector consist of 32 pairs of detector coils connected to a circuit that enables the preparation of persistent supercurrents and bond pads to connect to the SQUID input coils. The functions and layouts of these components are explained in this section.

3.3.1 Detection coils

As sketched in figure 3.1, the 64 individual MMC detection coils of each row are connected in series to form one large coil. When choosing a suitable coil geometry, four aspects should be considered:

- The coils have to feature a strong magnetic coupling to the sensors.
- The coils should be insensitive to the influence of external magnetic field changes and to the fields generated by the neighboring detection coils.
- The coils will supply the magnetic field needed to magnetize the sensors (see section 2.3). Therefore, there has to be a mechanism which enables the preparation of persistent supercurrents.

- The complexity of fabrication should be kept low. If a coil is interrupted somewhere due to a fabrication error, the readout scheme leads to the failure of two entire rows, each containing 64 pixels.

All the four criteria are fulfilled by the detector depicted in figure 3.3. The layout of its current carrying structures is summarized in figure 3.4. They consist of two wiring layers which are depicted in gray (first layer) and in transparent red (second layer). Both wiring layers are made from niobium and are therefore superconducting during experiments. For reasons of clarity, the separating insulating layers are not shown. The layers form the coils themselves, their connections to the SQUID bond pads and the electrical connections to the heat switches for preparing persistent currents. The detection coils are electrically identical to the equivalent circuit shown in figure 3.1, provided that the indicated connections are made to the input coils of the 32 SQUIDs. Two adjacent coils, connecting to the same SQUID are each set up as mirror images of each other resulting in different signal polarities. As depicted in enlargement b) and c), the coils feature meander shaped sections with a square area of $200\,\mu\text{m} \times 200\,\mu\text{m}$. The geometry and properties of meander coils were discussed in section 2.3.1. On each of the meander coils a sensor is placed, as to be discussed in section 3.4. This geometry is advantageous, since a meandering coil couples strongly to a planar sensor closely above it. However, the fragile geometry of the meanders with a pitch $p = 9\,\mu\text{m}$ between lines and a line width $w = 4.5\,\mu\text{m}$ over 11 turns makes them very susceptible to damage. To avoid one whole row pair becoming useless if a meander is interrupted by a fabrication error, a form of redundancy is created by connecting two similar meander coils in parallel under each sensor. With this geometry, the current flow under a sensor is only interrupted if both its meander coils are broken. In one direction, the 64 meander pairs under the 64 sensors of one row are connected by $35\,\mu\text{m}$ wide lines. The meanders and these connections are structured in the fist wiring layer, while the other direction of the entire coil is structured in the second wiring layer. The return line having a width of $30\,\mu\text{m}$ sits on top of the connections between the meanders. The cross section of the two lines, including the separating insulation layers is depicted in figure 3.5. Here, the two wiring layers are shown in gray and red to stay consistent with figure 3.4, while the insulation layers are depicted in black and blue. This geometry drastically reduces the parasitic inductance of the connections between meanders, since the created conductor loops do not enclose a significant area. To shield the meandering coils themselves from external magnetic fields, the return line is routed around them, creating a closed superconducting shielding ring which can be seen in figure 3.4 b) and c). As to be discussed in section 3.4.1, gold will be layered over one bracket of this ring as part of the gold thermalization structures. To avoid contact with the non-insulated second wiring layer, this bracket is structured in the first wiring layer (gray) and is contacted with the rest of the return line through surfaces where the

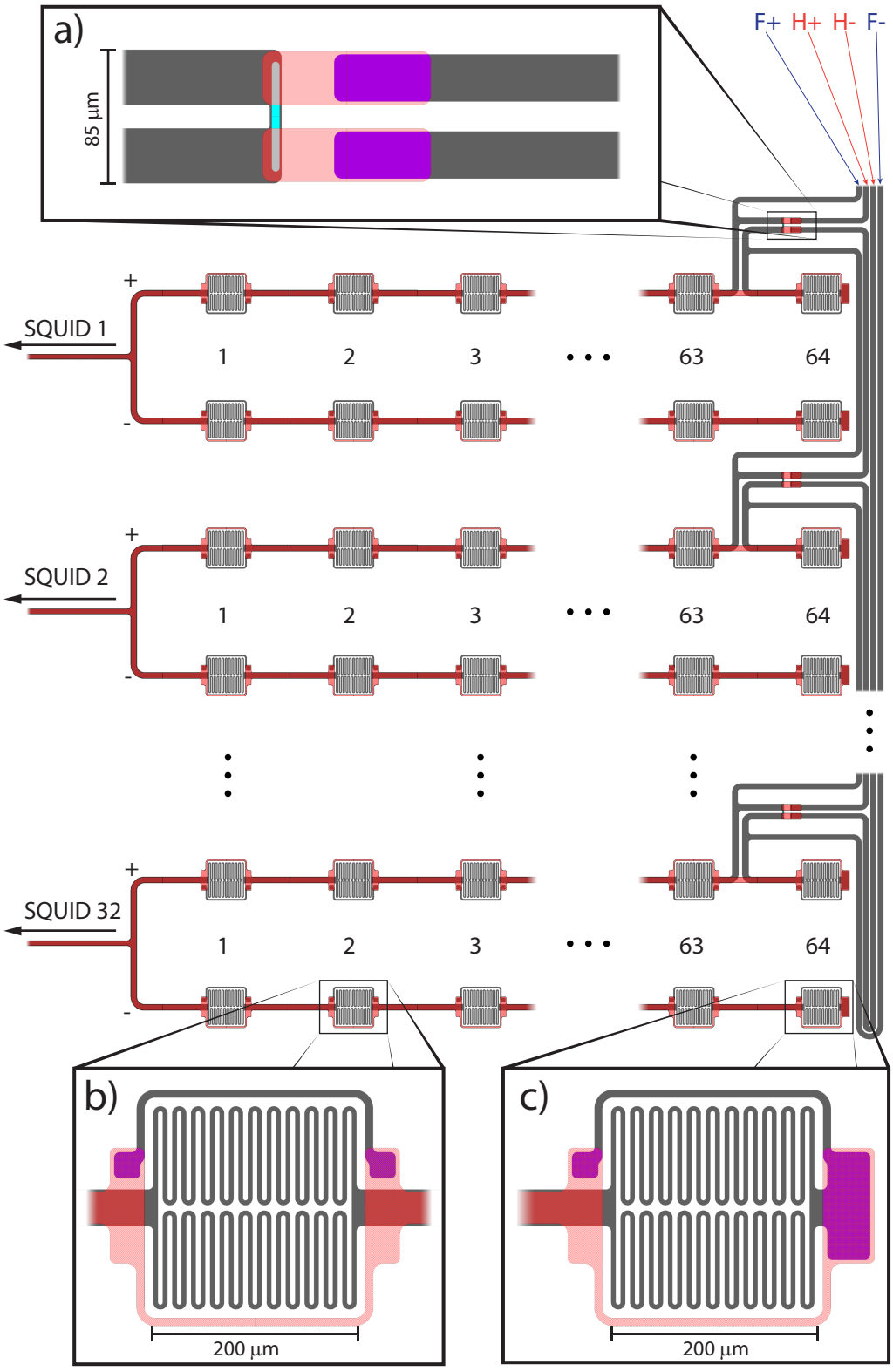

Figure 3.4: Cropped view of the current-carrying detector structures. It depicts the lower wiring in gray, the upper wiring in transparent red and the heater resistors in light blue. Enlargement a) shows a heater resistor, b) the wiring of one of the 63 standard pixels of a row, and c) the wiring of the last pixel of a row. The enlargements demonstrate areas of electric contact between the wiring layers in purple. The field and heater lines are labeled F+/- and H+/-.

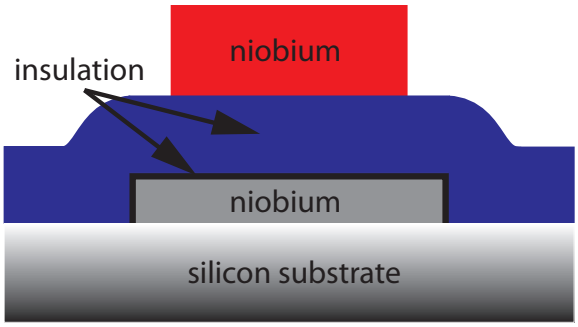

Figure 3.5: Cross section of the two niobium lines between meander coils, separated by insulation layers depicted in blue and black. The insulations are omitted in figure 3.4 for clarity.

two insulation layers on the first wiring layer are omitted. These "vias" are depicted as purple surfaces in the enlargements of figure 3.4. The same technique also joins the superimposed lines at the right end of each row, as depicted in enlargement c). The inductance of one detection coil pair can be approximated using equation 2.7 as $L_{\text{channel}} \approx 18\,\text{nH}$, when neglecting the connections between the meanders.

3.3.2 Persistent current switches

As explained in chapter 2.3, the paramagnetic sensors of MMCs need to be magnetized inside a magnetic field. For the detector presented here, this field emerges from a persistent current that is prepared inside the superconducting detection coils. As can be seen from the readout scheme in figure 3.1, two adjacent interconnected coils form a single conductor loop. Therefore, a supercurrent needs to be prepared inside each of the 32 coil pairs. Each coil pair includes a current switch on its right end as shown in figure 3.4 a). All 32 coil pairs including each switch are connected in series. This resulting field circuit is labeled F+/-. Each switch consists of a taper in the lower wiring line, on which an Ohmic resistor R is placed, as enlarged in figure 3.4 a) (light blue). On both sides of the heater, separate lines form a second circuit, connecting all the 32 resistors in series (labeled H+/- in figure 3.4). The current preparation process and the two circuits are schematically sketched in figure 3.6. When a field current I_{F} is initially pushed through the field circuit, it takes approximately the path depicted red in figure 3.6 a), as it has a much smaller inductance. If at the same time, a sufficiently large current I_{H} flows through the heater circuit, the voltage drop over each resistor heats the tapered superconducting line beneath it above the transition temperature of niobium. This causes it to become normal conducting. Consequently, I_{F} will take the remaining superconducting path and thus flow through the detection coils, as depicted in figure 3.6 b). Disabling the heating current before the field current closes the 32 superconducting loops again, thus leading to a persistent current I_{F} inside each detection coil, as depicted in figure 3.6 c).
The dimensions of the persistent current switches are chosen very similar to switches

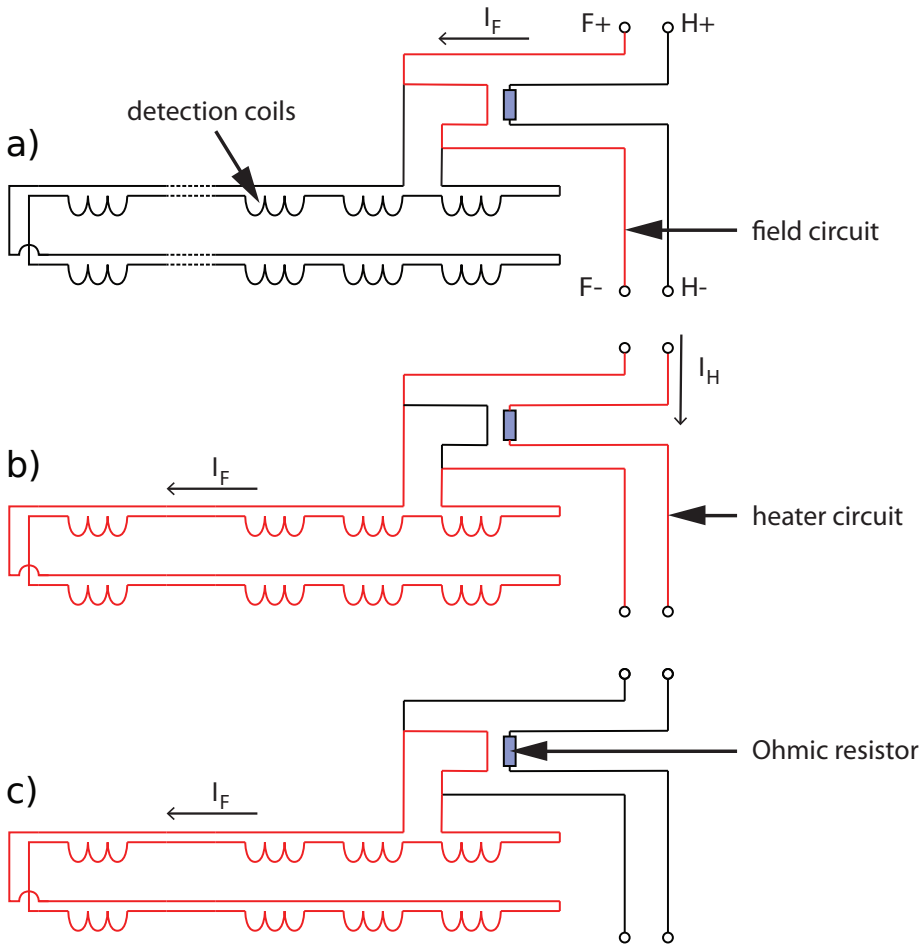

Figure 3.6: Schematic view of the preparation of persistent supercurrents inside the detection coils. Current-carrying lines are depicted in red, lines without current in black.

used in [Gas17], [Gei20] and [Sch21], as their functionality has been confirmed. The switches are placed as far away as possible from the other niobium conductors to avoid accidentally heating them up as well. However, care was taken to place the heaters under the absorbers, but not under one of the gaps between two absorbers. In this way, a particle hit in the heating resistor is avoided which could also cause the superconductivity to break down.

3.3.3 SQUID bond pads

On the left edge of the chip, the detection coil pairs depicted in figure 3.4 connect to bond pads. The pads are organized into blocks of four positive and four negative contacts each, as shown in figure 3.7. The bond pads for the lower niobium lines are centered, whereas the contacts for the upper niobium lines are symmetrically split into two parts. All bond pads are structured in the lower niobium wiring layer,

with no insulation layers on top. The electrical contacts between the two niobium layers are colored purple in the enlargement. This block geometry will be used with 3.2 mm × 3.2 mm square SQUID chips. Each chip contains four separate SQUIDs which are fabricated at KIP. Each block mirrors the connections on a SQUID chip, as depicted in figure 3.7. The bond pads facing each other in this way are later to be superconductively connected by thin aluminium wires, depicted in blue. Only two or three detection coil pairs are connected to each bond pad block instead of four, as depicted in figure 3.3. This creates a form of redundancy, enabling the use of SQUID chips with only two or three working SQUIDs. In total, 12 SQUID chips are required to fully operate the detector, 4 of which must have at least two working channels and 8 of which must have at least three working channels.

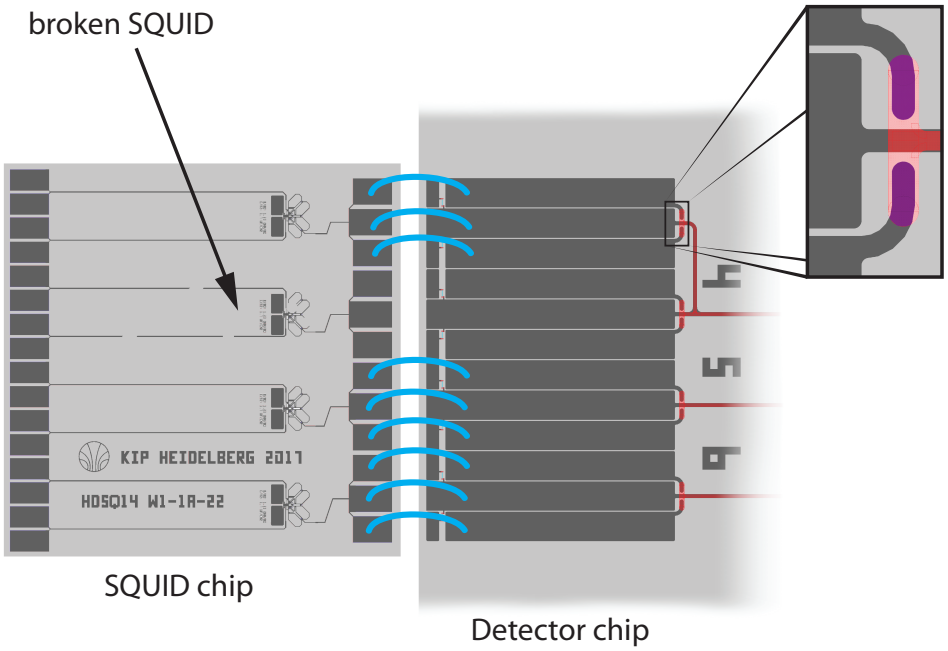

Figure 3.7: Exemplary view of one bond pad block connected to a chip with four SQUIDs. Three working SQUIDs are connected to the detector chip via thin aluminium wires. Due to the redundancy of one bond pad pair the SQUID chip can still be used despite of a broken channel. The enlargement shows the connection of the bond pads to the detection coils. On the detector chip, the niobium structures are depicted in gray and transparent red, electrical contacts in the enlargement in purple and aluminium wires in blue.

3.4 Sensor thermalization via gold structures

On top of the meandering parts of the detection coils, discussed in section 3.3.1 are the sensors of the 64 × 64 MMCs, separated by an insulation layer. Figure 3.8 shows a transparent view of the sensors in blue, above the niobium lines in gray and red. The material of the sensors will be the paramagnetic Ag:Er alloy, discussed in section 2.2, with an erbium concentration of approximately 395 ppm. The sensors are structured as rounded squares with an edge length of 200 μm. They each possess three protrusions that cover the brackets of the rings around the meanders which are structured in the lower wiring layer (gray). These protrusions are to ensure a proper thermal connection between the sensors and gold structures, depicted in light and dark orange. The gold structures implement the decay time discrimination between columns intended by the readout scheme (see section 3.1). For this purpose, they form thermal links between the sensors and a thermal bath with different thermal conductivities between all 64 sensors in the same row, as shown in figure 3.2. The technical details of this implementation are discussed in the following.

3.4.1 Decay time discrimination

Part of the readout scheme is the discrimination of MMC pixels within the same row via 64 different signal decay times. When choosing the range over which the decay time is varied, three aspects should be considered:

- The decay time of the fastest MMC should not be too short. Otherwise its energy resolution will decrease as described by equation 2.30.
- The decay time of the slowest MMC should not be too long. Otherwise the frequency with which the detector can measure particle hits within the same row will decrease.
- The difference in decay time between all MMCs should be large enough to distinguish between columns when evaluating the measured data.

To fulfill these three requirements, an equidistant interval $\Delta\tau$ between two successive decay times τ_i and τ_{i+1} is best. Figure 3.8 shows how to implement this. Each sensor belonging to the two mirrored rows corresponding to one SQUID, is connected to a common thermalization pad (depicted in light orange) by a golden link (depicted in dark orange). The links have a width of $w_{\text{link}} = 60\,\mu$m and a length that decreases linearly from $l_1 = 125\,\mu$m for the sensor to the far left to $l_{64} = 24.2\,\mu$m for the sensor to the far right in increments of $\Delta l = 1.6\,\mu$m. Enlargement a) and b) in figure 3.8 show the sensors with the longest and shortest gold links. The links consist of a

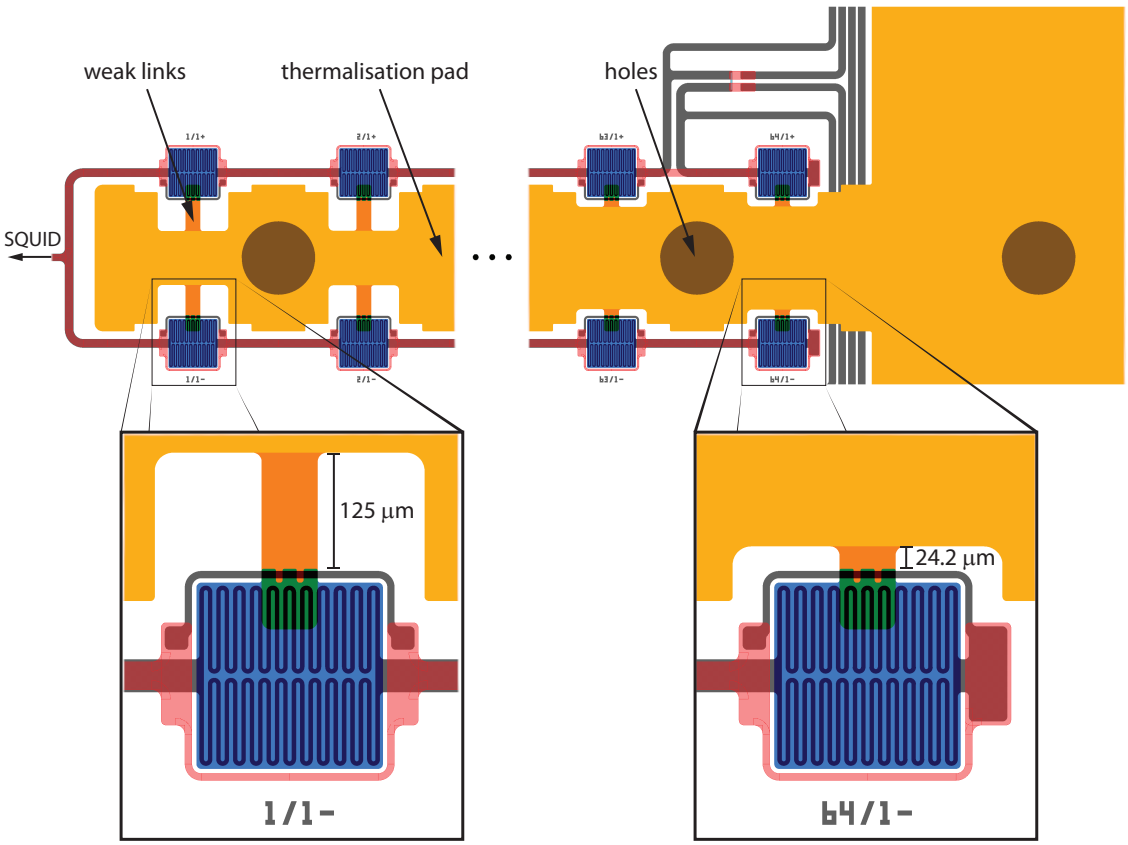

Figure 3.8: Excerpt from the design drawings of one pixel row pair. Depicted are the niobium structures in gray and transparent red, gold surfaces in light and dark orange, sensors in transparent blue and gold filled holes through the wafer in brown. Absorbers and insulation layers are omitted for clarity. The gold links to the sensors get shorter from left to right, in increments of $\Delta l = 1.6\,\mu$m. Enlargement a) shows the sensor with the longest gold link, enlargement b) the sensor with the shortest gold link.

$h_{\mathrm{link}} = 100\,$nm thick layer of sputter deposited gold with $RRR_{\mathrm{Au,\,sp}} \approx 2.5$. For the thermalization pads this thin gold film is covered with a $h_{\mathrm{pad}} = 2\,\mu$m thick layer of electroplated gold with $RRR > 20$. The thermalization pad has the function of a thermal bath of constant temperature, as depicted in blue in figure 3.2. Whether this assumption is reasonable is discussed in the next section.
The direct thermal coupling between sensors and cryostat through the dielectric and superconducting layers beneath the sensor and the $380\,\mu$m thick silicon wafer is very poor due to the absence of conduction electrons and multiple Kapitza resistances, as discussed in section 2.6. Consequently, the thermal conductivity $G_{i,\mathrm{link}}$ of the metallic gold links dominate the thermal connection G_i between sensor i and the thermal bath (see figure 3.2), so that $G_i \approx G_{i,\,\mathrm{link}}$ applies. $G_{i,\,\mathrm{link}}$ can be estimated

using equations 2.37 and 2.38 as

$$G_{i,\,\mathrm{link}} \approx LT\sigma_{\mathrm{Au,\,sp}}(4.2\,\mathrm{K})\frac{h_{\mathrm{link}}w_{\mathrm{link}}}{l_i} = LT\sigma_{\mathrm{Au,\,sp}}(300\,\mathrm{K})RRR_{\mathrm{Au,\,sp}}\frac{h_{\mathrm{link}}w_{\mathrm{link}}}{l_i}\,. \quad (3.1)$$

Here $\sigma_{\mathrm{Au,\,sp}}(T)$ is the thermal conductivity of sputter deposited gold. From this, the signal decay time of the i-th column follows from equation 2.26 as

$$\tau_i = \frac{C_{\mathrm{tot}}}{LT\sigma_{\mathrm{Au,\,sp}}(300\,K)RRR_{\mathrm{Au,\,sp}}\frac{h_{\mathrm{link}}w_{\mathrm{link}}}{l_i}} \propto l_i\,. \quad (3.2)$$

Assuming that the thermalization pad functions as an ideal thermal bath, the resulting decay times range from $\tau_1 = 3.1\,\mathrm{ms}$ to $\tau_{64} = 0.6\,\mathrm{ms}$, in increments of $\Delta\tau = 40\,\mu\mathrm{s}$. A table showing the expected decay times for all 64 detector columns in this approximation can be found in appendix A.1.

Columns with successive decay times are geometrically adjacent to reduce the error-proneness of the readout scheme. If the distinction between two or more neighboring decay times becomes unclear, for example due to fabrication errors of the gold links, the column-wise resolution of the detector is only reduced at the location of the error instead of losing the complete spatial information of the signal in question.

3.4.2 Thermal bath

The calculation of the decay times in equation 3.2 assumes that the links connect the sensors directly to a thermal bath of constant temperature T_0, i.e. $G_i \approx G_{i,\,\mathrm{link}}$ in figure 3.2. This assumption is potentially problematic, since the heat capacity of the thermalization pads between two MMC rows is with approximately $C_{\mathrm{pads}} \approx 5 \times 10^{-11}\,\mathrm{J/K}$ only a factor of about 6 larger than the heat capacity of one single sensor and absorber with $C_{\mathrm{tot}} = 8.1 \times 10^{-12}\,\mathrm{J/K}$. Therefore, in the case of a large energy input onto the detector per unit of time, due to the incident particle beam, it is questionable to what extent the thermalization pads heat up and whether this temperature increase is sufficiently homogeneous through the entire pad. In particular, the potential temperature inhomogeneity could disturb the decay time distinction, since the thermal conductivity of solids at low temperatures strongly dependent on temperature (see section 2.6). Additionally, a temperature increase of the chip would worsen the signal-to-noise ratio of the detector.
The seemingly obvious solution to this problem would be to increase the heat capacity C_{pads} of the thermalization structures between the rows i.e. by an increase in layer height. This is not favorable, however, as a gold layer thicker than $2\,\mu\mathrm{m}$ could break the wafer due to the different thermal expansion of gold and silicon. Switching to a different layer material with a significantly higher specific heat capacity than electroplated gold, such as the sensor material Ag:Er, is not advisable either. The

many intrinsic defects associated with it would significantly restrict thermal conduction which would potentially result in further temperature inhomogeneity.
Instead, good thermal contact should be established between the thermalization structures and the next actual thermal bath which will be the detector holder consisting of a massive copper block beneath the detector chip. Assuming the copper holder as a thermal bath is justified. Its heat capacity is infinitely large in comparison to the chip and it is in good thermal contact to the coldest stage of a dilution refrigerator. A very similar setup was already used for the MOCCA detector in [Sch21]. In the following, two options of heat transfer between the thermalization pads and this thermal bath are presented. They improve upon the insufficient coupling via the wafer itself.

Heat sinking via gold wires

Firstly, the thermalization pads between the MMC rows are extended on their right side and connected. The created gold surface covers the edges of the wafer and is only recessed for the bond pads, as shown in figure 3.3 of the whole detector. On the right edge of the chip they can be connected to the copper holder beneath the chip by a large number of gold wires. Therefore, if enough power is incident on an MMC to locally increase the temperature of its corresponding thermalization pad, the heat spreads diffusely throughout the whole gold structure of the row. If the heat dissipation through the wafer is insufficient, the left hand side of the chip will heat up while its right side stays at the temperature T_0 of the copper block. This effect is further amplified by the inevitable Joule heating of the 32 SQUIDs

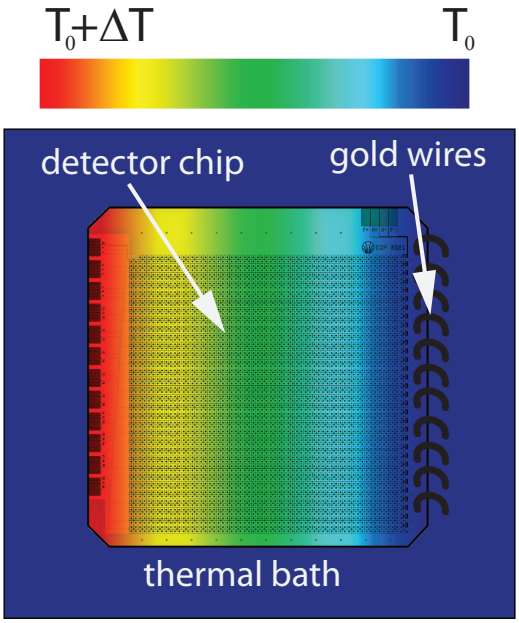

Figure 3.9: Sketch of the temperature distribution on the chip due to absorbed particles and SQUID heating if the chip is coupled to the thermal bath via a sufficient amount of gold wires on the right side of the chip.

left of the detector chip. Consequently, a temperature gradient from slightly higher temperatures $T_0 + \Delta T$ on the left hand side to T_0 on the right hand side will form, as sketched in figure 3.9. While this is not a homogeneous temperature distribution, it does not interfere with the decay time discrimination. This is because the weak links to the sensors are arranged in increasing coupling strength from left to right, as shown in figures 3.8 and 3.2. According to thermodynamics, heat always flows from higher to lower temperatures. Sensor i would therefore be connected to the thermal bath by the conductivity of its weak gold link $G_{i,\mathrm{link}}$ and the conductivity $G_{i,pad}$ of the thermalization pad section between sensor i and the right edge of the chip. As both $G_{i,\mathrm{link}}$ and $G_{i,pad}$ get larger with increasing values of i,

$$G_i = (G_{i,\mathrm{link}}^{-1} + G_{i,\mathrm{pad}}^{-1})^{-1} < (G_{i+1,\mathrm{link}}^{-1} + G_{i+1,\mathrm{pad}}^{-1})^{-1} = G_{i+1} \tag{3.3}$$

still applies and thus $\tau_i > \tau_{i+1}$ still holds true as before.

While this design feature ensures the proper functionality for temperature differences ΔT across the chip which are small compared to T_0, a very large temperature gradient can lead to other problems. Due to $C_{\mathrm{metal}} \propto T$, the signal height of an MMC decreases approximately linearly with rising temperature. Therefore, if ΔT is not small compared to T_0, the pixels will behave significantly less sensitive the further left they are located on the detector. Furthermore, although the order of the decay times remains unchanged, their absolute values do not. Accordingly, the detector has to be recalibrated with each new temperature gradient.
A superior option for establishing the thermal connection to the thermal bath are gold-filled holes through the wafer, as explained below.

Heat sinking via gold-filled holes

To prevent large temperature gradients across the detector chip, an optional design feature is a total of 1024 gold-filled holes running through the wafer. Figures 3.3 and 3.8 show the holes as brown circles. They each have a diameter of 300 μm and are arranged in a grid at intervals of 1400 μm below the thermalization pads. The holes are filled with electroplated gold and connect the pads through the wafer with a 2 μm thick layer of the Ag:Er sensor material on its backside, as sketched in figure 3.10. The large heat capacity of the paramagnetic Ag:Er material and the metal-on-metal contact to the copper holder, in addition to the previously discussed gold wires, promote a temperature of the thermalization pads very close to T_0 even for relatively large powers of incident particles. Therefore, this design feature should disable significant temperature gradients across the chip in most experiments. Hence, equation 3.2 applies for the calculation of decay times.
This second option of thermal contact is superior with regard to the final result.

However, etching and then filling thin holes through a 380 μm thick silicon wafer is difficult and is discussed in Chapter 4.

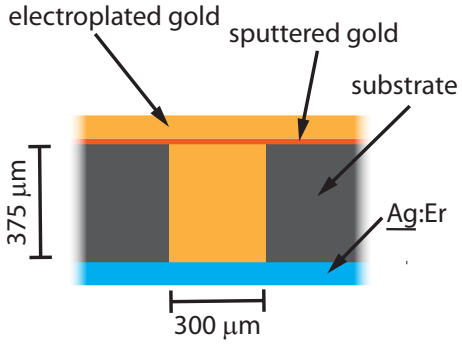

Figure 3.10: Sketched cross section of a gold filled hole through the substrate, connecting the gold thermalization surface on top with a Ag:Er thermal bath on the bottom of the chip. Layer thicknesses exaggerated.

3.5 Absorbers

Each of the MMC sensors discussed in section 3.4 is contacted to a square absorber. With an edge length of 698 μm and no rounded corners, the absorbers cover 99.4 % of the detection area, only leaving 2 μm gaps between the absorbers for thermal separation as shown in figure 3.11 a). Here, the absorbers show in transparent yellow to allow a view onto the underlying structures that have been discussed in the previous sections. The contact between absorbers and sensors is obtained via

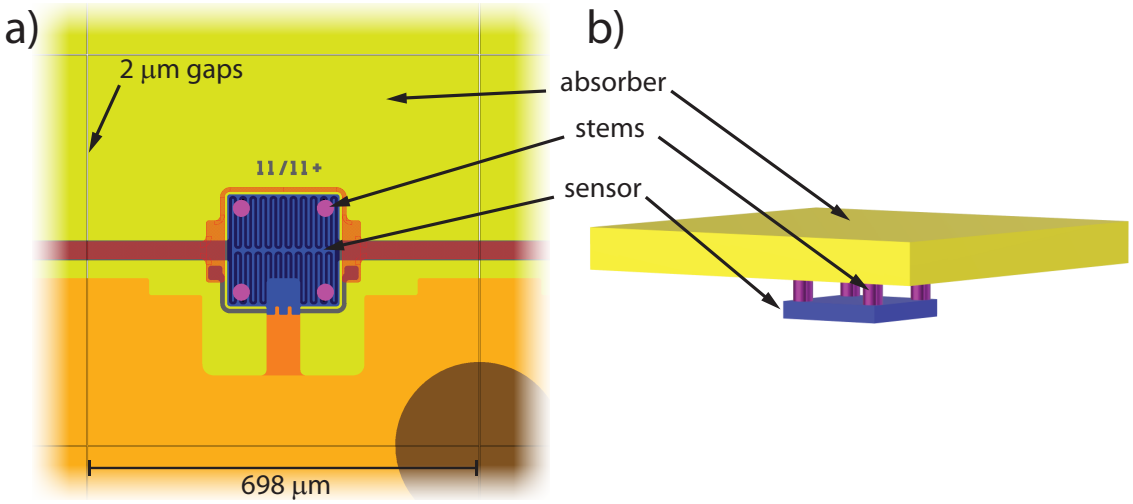

Figure 3.11: a) Design excerpt with transparently depicted layers of an absorber (yellow), connected by stems (purple) to a sensor (blue). b) Schematic side view of absorber, stems and sensor. Layer thicknesses exaggerated.

four stems which are fabricated from the same material as the absorber itself (see absorber layer in 3.1). The stems are colored pink in figure 3.11 a) while 3.11 b)

gives a schematic side view of an absorber connected to a sensor via the stems. This stem design has been chosen instead of a full-surface contact to prevent any phonons generated by the impact of an incident particle from passing through the sensor and into the substrate of the wafer, as they would not thermalize with the paramagnetic spin bath. Consequently their energy would not be detected as a magnetization change of the sensor and therefore be lost to the measurement.
The choice of the right absorber material was briefly mentioned in section 2.5. An in depth discussion can be found in [Gam19]. The first prototype of the detector will initially be characterized outside the CSR using radioactive sources. For this purpose, the absorber layer should be made of 4 μm thick gold, as gold is metallic, easy to process and good at stopping the 6 keV X-rays usually used for such tests. For the later detection of neutral molecule fragments, the fabrication of metallic layers with a high aluminium content or an element with a similar atomic mass should be explored (see [Gam19]) to minimize the loss mechanisms discussed in section 2.5.

3.6 Temperature sensitivity of the detector

As previously discussed, the detector organizes detection coils into pairs that connect to the same SQUID with different polarities. An advantage of this gradiometric setup is that temperature changes of the sensors which are identical in both coils negate each other. This means however that the detector temperature cannot be determined from the signal baselines. Since many properties of MMCs, first and foremost the height of detected pulses (since $C_{\mathrm{metal}} \propto T$), strongly depend on temperature, some kind of thermometer on the chip would be advantageous. To enable this without additional complexity, the leftmost two pixels in the top row of the detector can optionally be omitted, as shown in figure 3.3 of the whole chip layout. This breaks the symmetry of the two columns connected to the first SQUID, making its baseline signal dependent on the temperature of the spins inside the two sensors without mirror image. The price for this is the now larger and temperature dependent baseline as an additional noise contribution in the affected SQUID. For this reason, one of the outermost rows was chosen, as they should be less important for most measurements. Within these rows, the leftmost two pixels of the top row were selected. This enables the measurement of temperature gradients across the chip when thermally short-circuiting its right edge to the temperature T_0 of the thermal bath via gold wires, as depicted in figure 3.9. Furthermore, this places the temperature sensitive zone close to the SQUIDs which are the largest potential heat source due to their intrinsic Joule heating. Additionally, the placing does not interfere with a potential future combination of four identical detectors which is discussed in section 3.8.

3.7 Layer organization

After discussing the layout of the design, this section summarizes the properties of the layers which constitute its structures. Their function, material, thickness and covering order is summarized in table 3.1.

covering order	**layer**	**material**	**thickness** [nm]
0	substrate	Si	380000
1	lower wiring	Nb	250
2	isolation 1a	Ni_2O_5	32
3	isolation 1b	SiO_2	350
4	upper wiring	Nb	400
5	heater resistors	AuPd	160
6	thin gold structures	Au ($RRR \approx 2.5$)	100
7	thick gold structures	Au ($RRR > 20$)	2000
8	sensors	Ag:Er	1667
9	isolation 2	SiO_2	250
10	absorbers on stems	Au*	4000*

Table 3.1: Overview of the detector layers, in order of covering. *Material and thickness of the absorbers and stems is situational as discussed in section 3.5.

The current-carrying structures are organized in two overlapping wiring layers made from niobium (lower and upper wiring in table 3.1). To avoid short-circuits between the two superconducting layers, the structures of the bottom niobium layer are oxidized, resulting in an approximately 32 nm thick[2] Nb_2O_5-coating (isolation 1a in table 3.1). To ensure even better insulation, the bottom layer structures are additionally covered by a SiO_2-coating (isolation 1b in table 3.1), on which the structures of the second niobium layer lie. Both insulation layers are left out at deliberate contact points between the two wiring layers. The structures of wiring layers consist of the detection coils, the bond pads for connecting the coils to the SQUID-chips and the circuit enabling the preparation of a persistent super-current inside the coils. For this purpose Ohmic heater resistors, made from an AuPd-alloy, are required (heater resistors in table 3.1).
A central aspect of the readout principle is the variation of decay times. The thermalization surfaces needed to implement this idea are structured in a 100 nm thin gold layer of poor crystalline purity and a 2 μm thick gold layer of high crystalline purity (thin and thick gold structures in table 3.1). The 4096 sensors of the MMCs are structured in a 1.7 μm thick silver layer which is doped with 395 ppm erbium

[2]measured ad KIP 2021 for ECHo100kv1.1w1 3D1

(sensors in table 3.1). All structures of the layers described so far that need to be electrically or thermally insulated are covered with another SiO_2 insulation layer (isolation 2 in table 3.1) to avoid short-circuits. Finally, the sensors are connected to absorbers by stems, both of which are structured from the same situational material (absorbers on stems in table 3.1), as discussed in section 3.5.
An Overview over the fabrication of these layers is given in chapter 4.

3.8 Potential quadrupling of spatial resolution

All the essential structures of the right and bottom edges of the detector chip are located under the absorbers, while the bond pads on the left and top sides are arranged in such a way that there is enough space to mount the detector on top of an appropriate future setup using these two sides alone. This makes it possible to connect four identical detectors to form a closed 8.96 cm × 8.96 cm detection area with 16384 pixels, by cutting and arranging the chips as depicted in figure 3.12. This setup requires 128 SQUIDs for a complete readout and relies on the thermalization holes described in section 3.4.

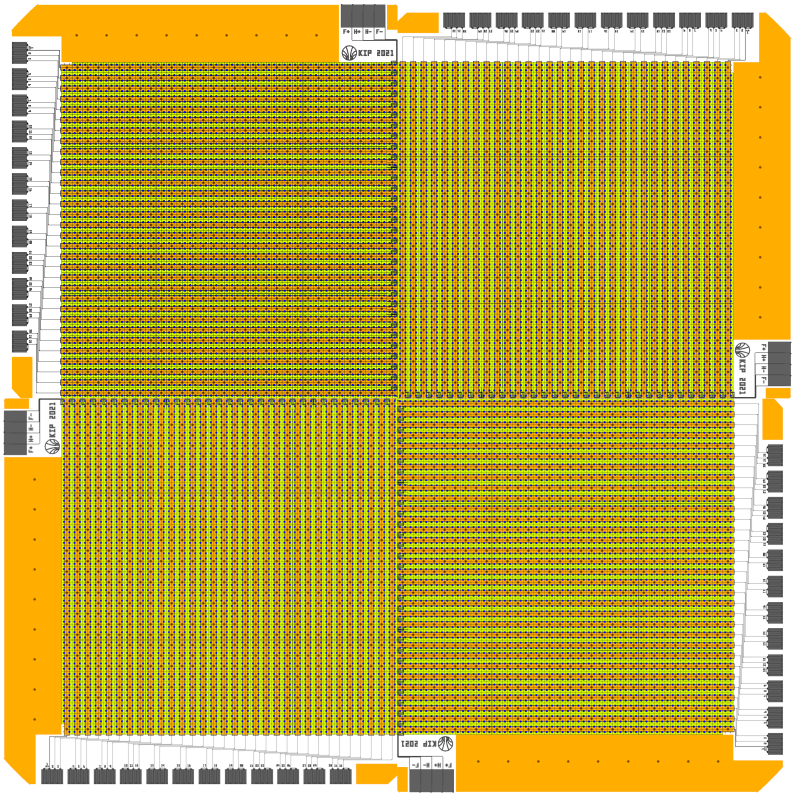

Figure 3.12: Schematic view of four identical chips, appropriately cut and joined together, resulting in an 8.96 cm × 8.96 cm detector area, containing 16384 pixels.

3.9 Optimization of design parameters

The presented design aims to build an MMC based detector that can energetically and spatially resolve neutral molecule fragments with kinetic energies up to 300 keV at the CSR. While MMCs can be optimized to achieve energy resolutions of only a few eV ([Fle09],[Por14], [Kem18]), this is neither necessary nor possible for this detector. In many experiments energy resolutions of $\Delta E_{\text{fragment}} < 1\,\text{keV}$ are already sufficient to determine the fragment mass with a precision of $\Delta m_{\text{fragment}} \approx 1\,\text{u}$, assuming a linear dependence

$$\Delta m_{\text{fragment}} \approx m_{\text{ion}} \frac{\Delta E_{\text{fragment}}}{E_{\text{ion}}} \,. \tag{3.4}$$

Here m_{ion} and E_{ion} are the mass and kinetic energy of the ionic molecule before the recombination reaction.
Furthermore, even if the MMCs of the detector were to be optimized with respect to the intrinsic energy resolution as calculated in 2.30, additional effects specific to the absorption of massive particles like backscattering or the creation of lattice defects upon absorption (see section 2.5) would worsen the actual energy resolution. Therefore, for the presented detector the optimization of the intrinsic energy resolution given by equation 2.30 is secondary to the spatial resolution which is much harder to achieve. This is why the readout scheme deliberately sacrifices energy resolution to simplify the operation of the detector. Most of the design decisions within the 64x64 MMCs themselves, such as the shape and area of absorbers, coils and sensors, are also not chosen for an ideal energy resolution but derived mainly from geometric requirements for a large-area pixel array and with manufacturing aspects in mind. Of the remaining parameters that have no influence on the spatial properties of the detector most cannot be chosen freely either. For example, the erbium concentration within the sensor material is fixed to 395ppm by the available targets for sputter deposition. The only parameter that should be optimized purely in terms of energy resolution is the sensor height h_{s}. A previously mentioned simulation script developed by [Her21] and [Sch00, Fle03, Fle05] was used for this purpose. Assuming that the detector is operated at a temperature of 20 mK and 4 μm thick gold absorbers are used as discussed in 3.5, the optimal height of the sensors is numerically calculated as $h_{\text{s}} = 1,68\,\mu\text{m}$ for a persistent current of 70 mA inside the detection coils. The combined parameters of the design then lead to an expected intrinsic energy resolution of $E_{\text{FWHM}} \approx 40\,\text{eV}$ for the fastest decaying pixel column of the detector. All other columns are slightly better resolved due to longer decay times, as apparent from equation 2.30. In this simulation result only the noise sources discussed in section 2.36 were considered. In particular, the additional effects inherent to the absorption of neutral particles (see section 2.5) were not taken into account here.

4. Detector fabrication

The detector presented in this thesis will be fabricated in layers of planar structures on a 3 inch silicon wafer. The layouts and functions of the different detector components were discussed in the previous chapter. Almost all structures are designed on a sub-mm-scale scale in the plane of the wafer, requiring a fabrication precision of about 1 μm. This is necessary because larger structures would have a direct negative effect on the calorimetric properties of the detector due to the resulting larger heat capacities. To achieve the necessary precision, the detector is therefore microfabricated in the institute's own cleanroom. This chapter briefly summarizes the most important fabrication processes and gives an overview of the steps in the production of the detector . It then discusses two manufacturing challenges related to the large size of the chip. Finally, the manufacturing process and advances in the fabrication of gold-filled holes through the wafer are presented.

4.1 Fabrication processes

The structures of the detector are organized in 10 different layers. Their materials, thicknesses and functions were discussed in section 3.2. The detector will be fabricated on a 3-inch silicon wafer with a thickness of about 380 μm which is covered with a 255 nm thick layer of thermal SiO_2. Most of the subsequent material layers are sputter deposited onto the wafer using either a DCA[1] or PREVAC[2] sputtering system. The layers are structured by lithographic processes involving photoactive resists. The resist masks are patterned in an MLA 150 lithography tool made by Heidelberg Instruments[3]. Here, the desired part of the design is directly written into the resist by lasers which alter the resists chemical structure. The resist is then developed in an alkaline solution which removes the altered or unaltered parts, depending on the resist. The two main lithographic processes used in fabrication are:

Etching processes: A layer of material on the wafer is covered by a light-sensitive resist. The resist layer is subsequently structured as described above, remaining only on the desired components. Finally, the parts of the initial material layer which are not protected by the remaining resist are etched away by chemical or physical dry etching processes. A PlasmaPro 100 Cobra etching system by Oxford Instruments

[1]DCA MTD 620, DCA Instruments Oy, Vajossuonkatu 8, 20360 Turku, Finland.
[2]PREVAC sp. z o.o.,Raciborska 61, 44-362 Rogów, Poland
[3]Heidelberg Instruments Mikrotechnik GmbH, Mittelgewannweg 27, 69123 Heidelberg

Plasma Technology[4] is available for dry etching processes. Here, the wafer is placed into a vacuum chamber where it can be exposed to various plasmas. Generally, a distinction is made between chemical and physical etching processes. In the former, a plasma reacts chemically with the material, resulting in isotropic etching. In physical etching, the atoms are knocked out of the material by ions that are accelerated onto the wafer from above. Physical etching is therefore anisotropic and can also remove chemically very inert materials.

Lift-off processes: In a first step, the wafer is coated with a resist layer. The resist is then patterned, remaining everywhere on the wafer except on the desired structures. A layer of material is then sputter deposited onto the wafer. Finally, the resist mask is dissolved which also removes the overlying material, leaving only the desired structures.

4.2 Fabrication overview

Table 4.1 shows an overview of the fabrication steps. Table 3.1 lists the material and thickness of the manufactured layers. The layer name column lists the names of the layers in the design file and serves as a reference for later production; it is not important for understanding the manufacturing process.

First of all, niobium is sputter deposited onto the blank wafer with a thickness of 250 nm. This layer is then etched, creating the first layer of detector wiring discussed in section 3.3 as well as some additional links. These links electrically connect all the structures of the first niobium layer so that they can be anodized in the second fabrication step. For this purpose, all surfaces that are not to be insulated, such as bond pads and future connections to the second layer of wiring (vias), are covered with resist. The remaining unprotected parts of the structures are then oxidized by anodization, resulting in a 32 nm thick Nb_2O_5 insulating layer in the second step. The anodization links between the structures are etched away in the third step. Subsequently in step four, the remaining niobium 1 structures are covered with another 350 nm thick SiO_2 insulation layer in a lift-off process, again only covering parts of the structures which need to be electrically insulated.
The fifth manufacturing step adds the heating resistors which were discussed in section 3.3.2. To this end, a 5 nm thick layer of sputter deposited titanium as a bonding agent and the sputter deposited AuPd alloy with a thickness of 160 nm are structured at the appropriate areas by means of a lift-off process.

[4]Oxford Instruments Plasma Technology, Yatton, Bristol, UK

For step six, the second niobium layer with a thickness of 400 nm is sputtered onto the now partially electrically insulated first niobium layer and structured by a lift-off process.

Step	**Structures**	**Layer name**	**Process**
1	lower wiring structures with annodization links	Niobium 1	sputter deposition, dry-etching
2	anodization of lower wiring structures	Isolation 1a	anodization
3	removal of anodization links	NbEtch	dry-etching
4	SiO2 insulation layer	Isolation 1b	sputter deposition, lift-off
5	fabrication of heater resistors	Heater	sputter deposition, lift-off
6	upper wiring structures	Niobium 2	sputter deposition, lift-off
7	removal of thermal SiO2 beneath Gold Pads	ThermalLinkGalv	dry-etching
8	gold 1 thermalization structures	ThermalLink	sputter deposition, lift-off
9	gold 2 thermalization structures	ThermalLinkGalv	electroplating, resist
10	optional gold filled thermalization holes	Holes	special*
11	sensors	Sensor	sputter deposition, lift-off
12	SiO2 Insulation layer	Isolation 2	sputter deposition, lift-off
13	stems	Stems	only resist
14	absorbers	Absorber	sputter deposition or electroplating, dry-etching, resist removal

Table 4.1: Overview of fabrication steps. Listed are the fabrication step sequence, the structures in the fabricated layer, the corresponding layer name in the design file and the processes during the step. *The fabrication of gold filled holes is discussed in section 4.3

The 7nth fabrication step is the removal of the thermal SiO_2 on the area of the

wafer that will later be covered by the electroplated gold surfaces. This is necessary for two reasons. Firstly, the thermalization pads are to serve as thermal baths for the sensors. Therefore, a good thermal bond with the silicon substrate is desirable. Secondly, in the optional 10th fabrication step, holes are etched from the backside through the entire wafer. Thus it is advantageous to remove the notoriously difficult-to-etch SiO_2 layer beforehand.

Using a 1-2 nm thick niobium layer as a bonding agent, the sputter deposited 100 nm thin gold surfaces are structured in the 8th step by a lift-off process.
In step nine, 2 μm of gold are electroplated onto the thin gold layer. The structures that are not to receive the additional gold layer are covered with a resist beforehand which is then removed again. Electroplated gold is used for this layer, as it achieves a high crystalline purity compared to sputter deposition and thus a good thermal conductivity of the thermalization structures.
The next production step 10 is the optional fabrication of gold-filled holes under the gold thermalization structures. Since their fabrication is not yet a standardized process and has been further developed in this thesis, it is discussed in detail in section 4.3.
In step 11, the sensors are sputter deposited and patterned by a lift-off process. In step 12, the entire wafer is covered with a second SiO_2 layer on top of a photoresist mask. This second insulating layer is patterned by another lift-off process and covers everything on the wafer except the sensors, the niobium bond pads and the gold surface which will be at the edge of the chip. The latter can therefore be connected to a thermal bath via gold wires, as described in section 3.4.2.

Finally, the absorbers on stems are fabricated in the two connected steps 13 and 14, as they actually consist of the same material layer. Figure 4.1 schematically shows the joint fabrication by means of a cross-section of the wafer. The substrate is covered with an approximately 5 μm thick resist into which the stems are structured as holes, as depicted in part a) of the figure. In part b), the absorber layer is sputter deposited onto the wafer. The resulting closed layer is then covered with another resist, leaving the future gaps between absorbers uncovered, as shown in c). The uncovered gaps are then used to etch away the absorber layer beneath in part d). After both resist layers have been dissolved in e), the absorbers remain, standing freely on the stems. Since high thermal conductivity of the absorbers and stems is advantageous, electroplating the absorber layer instead of sputtering might seem beneficial. Why this is not the case is explained in the next section which discusses some of the fabrication challenges that arise from the unusual chip size of the detector.

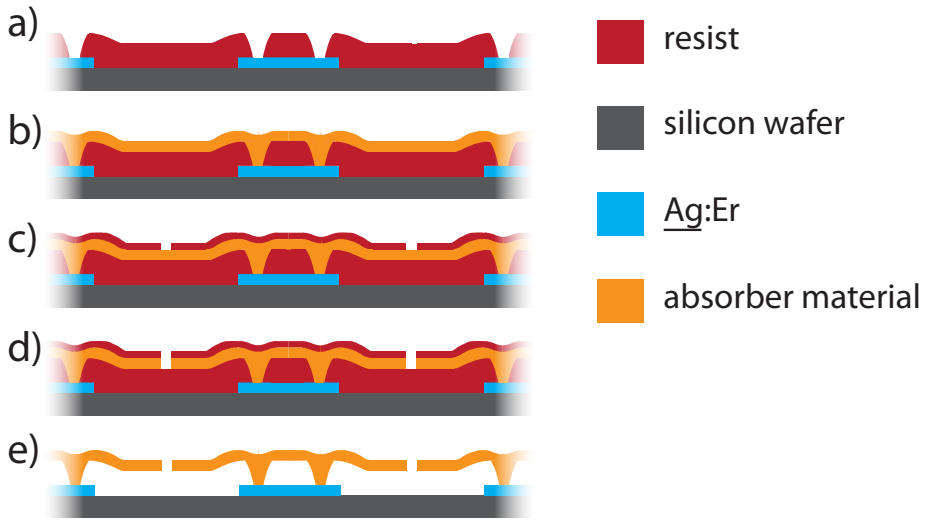

Figure 4.1: Schematic view of the absorber fabrication steps, visualized by a cross section of the wafer. a) stems structured in resist, b) deposition of absorber material, c) gaps between absorbers are structured in resist, d) etching and e) resist removal.

4.3 Special fabrication challenges

The detector presented in this thesis is unusually large compared to most other chips produced at KIP. This presents additional fabrication challenges which are discussed below.

Statistical error-proneness

The first challenge is a statistical consequence of the large size of the detector chip. Normally at KIP, several identical detectors are fabricated on one wafer which is then cut into several chips, e.g. the detectors used in [Gas17]. Chips containing critical fabrication errors are discarded. However, the design presented here fills the entire 3-inch wafer. Therefore, a single critical error during the long and tedious manufacturing process can easily destroy the entire wafer. To avoid this, almost all the structures on it that are important for more than one MMC pixel are either wider than about 30 μm and therefore less prone to fabrication errors, or provide some form of redundancy. For example, the chip's detection coils which would disable 128 pixels in case of an interruption, have two parallel meander coils under each sensor, as discussed in section 3.3. Only if both meanders under the same sensor are interrupted, two complete rows of pixels read out by the same SQUID will not work. Particular attention was paid to the electrical contact areas (vias) between the two layers of wiring, as they are prone to manufacturing defects. On the entire detector,

they are either wider than about 30 μm in both dimensions or comparatively uncritical for functionality.

Layer thickness inhomogeneity

The second challenge arises from the large detector scale combined with the potential inhomogeneity of the layer thicknesses on the chip. As part of the readout scheme (see section 3.1), the information in which column an absorber hit has occurred is encoded in the decay time of the detected signal. This requires fine-tuning of the decay times over the entire pixel array via 64×64 gold connections of 64 slightly different lengths. As described in section 3.4.1, the decay time of the i-th MMC in a row is calculated as the ratio of the combined specific heat $C_{\mathrm{tot}} = C_{\mathrm{a}} + C_{\mathrm{s}}$ of the absorber and the sensor to the thermal conductivity $G_{i,\,\mathrm{link}}$ of the column-specific thermal weak link to the thermal bath. From the geometry of the components, the signal decay time τ_i after an energy deposition on the pixel $\mathbf{x}$ that is part of column i on the chip is given as

$$\tau_i(\mathbf{x}) \approx \frac{c_{\mathrm{a},V} A_{\mathrm{a}} h_{\mathrm{a}} \alpha(\mathbf{x}) + c_{\mathrm{s}_V} A_{\mathrm{s}} h_{\mathrm{s}} \beta(\mathbf{x})}{g_{\mathrm{link}} w_{\mathrm{link}} h_{\mathrm{link}} / l_i \gamma(\mathbf{x})} \,. \tag{4.1}$$

Here, $c_{\mathrm{a},V}$ and $c_{\mathrm{s},V}$, A_{a} and A_{s} are the volume specific heat capacity and the area of the absorber and the sensor respectively, while g_{link}, w_{link} and l_i denote the material specific thermal conductivity of the gold link and its width and length. The numbers $\alpha(\mathbf{x})$, $\beta(\mathbf{x})$ and $\gamma(\mathbf{x})$ are the ratios between the layer heights of absorber, sensor and link at the pixel $\mathbf{x}$ of the array and their average heights h_{a}, h_{s} and h_{link} over the whole chip. Consequently, inhomogeneities of the layers do not alter $\tau_i(\mathbf{x})$, as long as all three layers have the same inhomogeneity, thus for

$$\alpha(\mathbf{x}) = \beta(\mathbf{x}) = \gamma(\mathbf{x}) \,. \tag{4.2}$$

Both the sensors and the gold links are sputter deposited onto the wafer. Since this always involves an unavoidable inhomogeneity, it should be identical for the sensor, link and absorber layers on the chip. Therefore, all three structures should be fabricated with identical sputtering setups, resulting in identical inhomogeneity on the chip and thus not changing the decay times of the MMCs. The fabrication of the absorbers by electroplating is therefore not advantageous.

4.4 Fabrication of gold-filled holes

Part of the detector design presented in this thesis are gold-filled holes through the wafer (see section 3.4). They intended to thermally connect the gold thermalization

structures on the front of the chip via the substrate to a layer of Ag:Er on the back of the chip. The process was first introduced to KIP in [Hen17, Sch19, Gam19] and was further developed in the framework of this thesis with help of the new PlasmaPro 100 Cobra OCPT[5] dry etching machine mentioned in section 4.1. The following summarizes the Bosch process for anisotropic dry etching of silicon and thereafter the principle of producing gold-filled holes through the wafer. Finally, the new advances are presented.

4.4.1 Bosch process

The holes through the 380 μm silicon wafer will be fabricated via the Bosch process. That is a three stage dry etching process in which passivation, physical etching and chemical etching steps are repeated again and again consecutively. The aim is to etch anisotropically, in this case perpendicularly to the wafer surface. Figure 4.2 schematically shows the three steps.

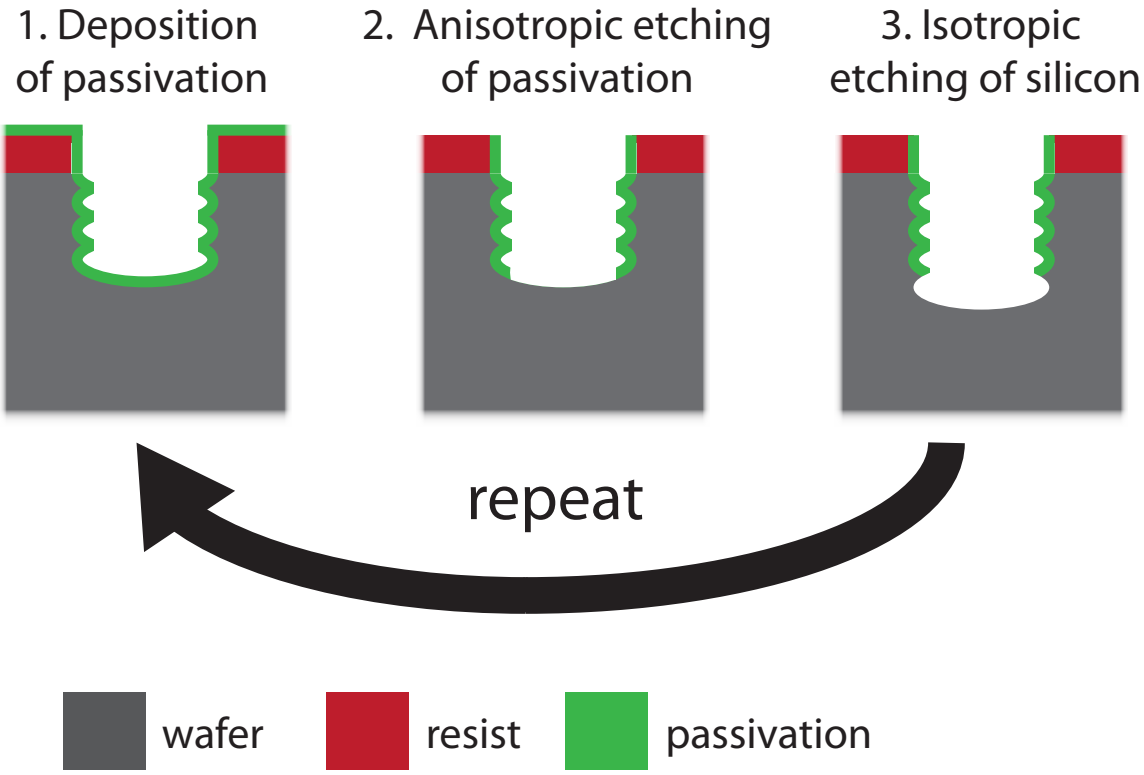

Figure 4.2: Schematic cross-section through the silicon wafer during the three repetitive steps that make up the Bosch process.

[5]Oxford Instruments Plasma Technology, Yatton, Bristol, UK

Before the process starts, the silicon wafer (depicted in gray) is masked with a resist (depicted in red) which covers those parts of the wafer that are not to be etched. The wafer is then exposed to a different plasma in each of the three steps. In the initial deposition step, C_4F_8 is activated to radicals and forms a polymer passivation layer (depicted in green) on the entire surface, i.e. on the mask as well as on the bottom and the vertical side walls of the hole (figure 4.2 1.). In the subsequent anisotropic etching step, a plasma of argon ions accelerated onto the wafer from above removes the in-plane part of the passivation layer again, leaving the side walls of the holes covered (figure 4.2 2.). Finally, a plasma of activated SF_6 containing F^- radicals etches the silicon isotropically, by forming gaseous SiF_4 (figure 4.2 3.). As the resist and the remaining passivation layer on the vertical side walls of the hole are chemically more inert than the silicon, almost only the bottom of the hole is attacked by the plasma. The etching is stopped after a short time and the three steps are repeated from the beginning. Consequently, a hole of any depth can be etched vertically into the wafer as long as the masking resist is thick enough to last throughout the process, as it too will inevitably be corroded by the plasma. The smoothness of the side walls depends on the duration of the isotropic etching step. Short isotropic etching leads to smoother walls, but also requires more repetitions of the three processes to achieve the desired depth.

4.4.2 Fabrication steps

As discussed in section 4.2, the fabrication of the gold-filled holes can be done as the 10th fabrication step, after the thermal oxide layer at the appropriate positions of the wafer is removed (both on the front and back of the wafer) and the two gold layers which make up the thermalization structures have been applied. Figure 4.3 schematically depicts the fabrication process. The structures on top of the wafer are coated with a protective resist layer, as the wafer is subsequently flipped (the front side of the wafer points downwards in figure 4.3). The holes are structured into a second resist layer on the backside of the wafer, as depicted in a). Here, a resist is used which is thick enough to endure the etching of the holes via the Bosch process, as depicted in b). In a next step, the gold surfaces on the front side of the wafer are contacted to the cathode of an electroplating setup. The holes are subsequently filled with electroplated gold, as depicted in c). After the electroplating process is completed, the resist on the backside of the wafer is removed. Subsequently, the protective resist coating on the front side of the wafer has to be renewed, as it is also removed in this step. Finally, a $2\,\mu$m thick layer of Ag:Er is sputtered onto the backside of the wafer, with niobium as a bonding agent. This layer is supposed to be part of a thermal bath as discussed in section 3.4.2. A thickness above $2\,\mu$m is not advisable, as this could break the chip during cooling due to the different

thermal expansion of silicon and Ag:Er. The Ag:Er is covered with a thin gold film via sputter deposition, to protect it from oxidization.

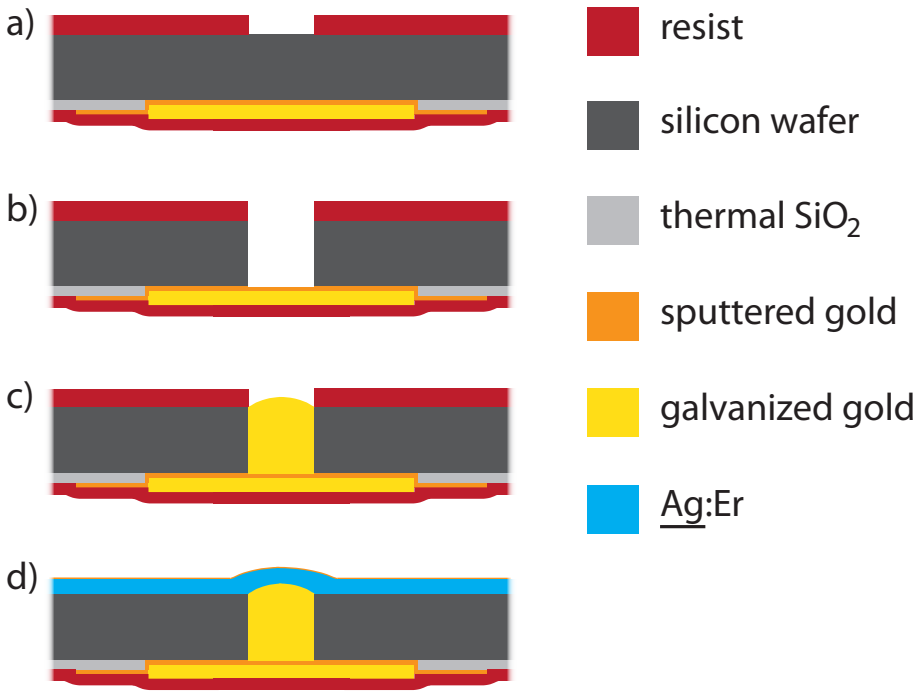

Figure 4.3: Cross section through the wafer during the fabrication of gold-filled holes. a) the finished structures on the wafer front side (pointing downwards) are coated with a protective resist layer. A mask for the holes on the back side of the wafer is structured in a 10 μm thick resist. b) The holes are etched using the Bosch process. c) The holes are filled with gold by using the gold layers on the front side as a cathode for electroplating. d) Ag:Er and a thin gold film are deposited on the backside, after removal of the resist on the backside.

4.4.3 Advances in fabrication

In the context of this thesis, steps a) and b) in figure 4.3 of the above-discussed fabrication of gold-filled holes in the wafer were developed. To this end, first a resist that would endure the Bosch-etching of 380 μm of silicon had to be found. This was realized by a 10 μm thick layer of the photo resist AZ4562 by Micro Chemicals[6]. A summery of the fabrication parameters can be found in appendix A.2. All tests were carried out on 2 inch silicon wafers, polished on one side and without a thermal SiO_2 layer.

[6]Nicolaus-Otto-Straße 39, 89079 Ulm, Germany

Figure 4.4 shows various microscope images of holes with a diameter of 300 μm which were etched through test wafers in the framework of this thesis. The holes are spaced at 1400 μm intervals in a grid pattern across the wafer, exactly as in the detector design. Part a) shows the cross-section of a hole. Part b) shows the cross section of

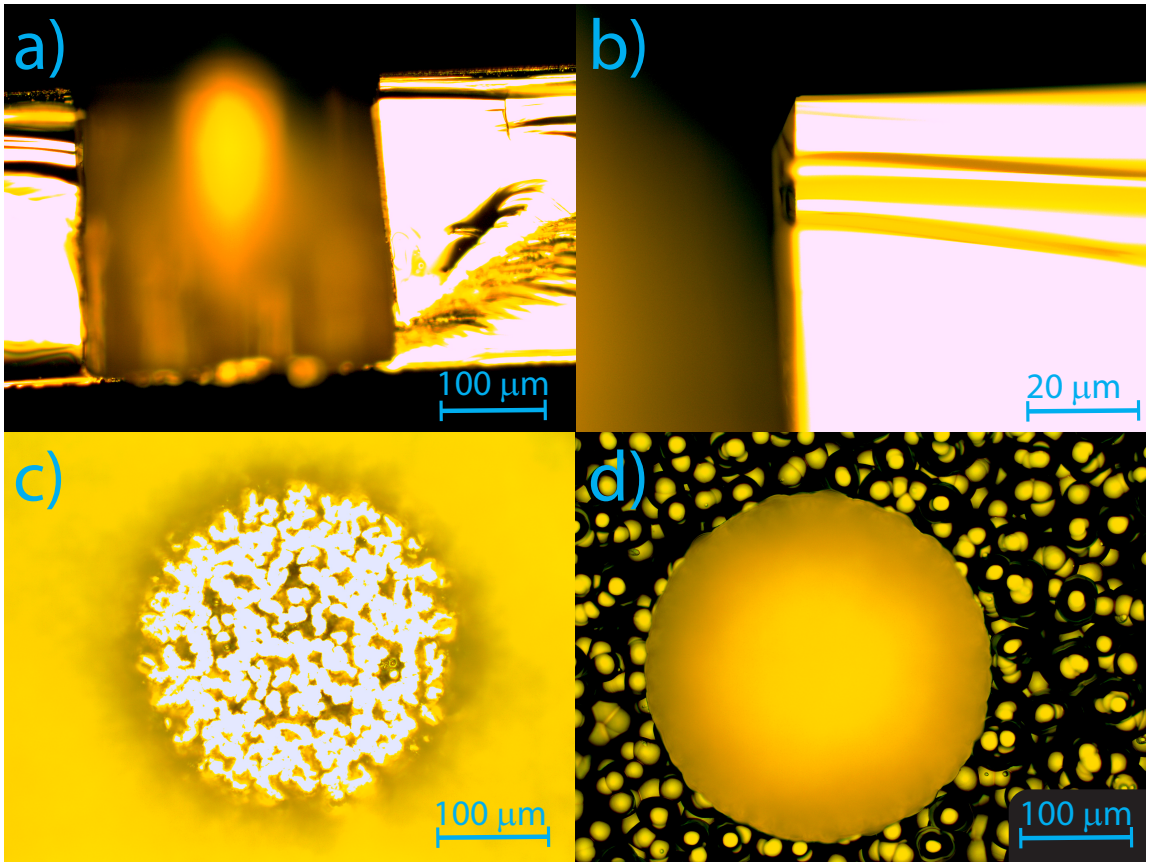

Figure 4.4: Microscope images of 300 μm diameter holes through a 380 μm thick silicon wafer, etched with the Bosch process. a) Cross-section through a hole. Side view of a wafer fragment, breaking edge in focus. b) Edge of a hole. Side view of a wafer fragment with breaking edge in focus. c) Top view of a hole with gold foil at the bottom, gold foil in focus. d) Same as c), but resist covered and unpolished surface of the wafer in focus.

the upper edge of a hole. As can be seen, the resist layer was thick enough to endure the etching process in order to avoid damage to the edge of the hole. Both images come from the same test wafer after 780 repetitions of the Bosch process. They were taken by breaking the etched wafer along the holes, with the focus on the break edge pointing upwards towards the microscope.
A 1 μm thick gold foil previously sputtered onto the polished front side of a wafer remains undamaged during the Bosch process. Photos of such a hole are shown in figure 4.4 c) and d). The pictures were taken from the unpolished back side of the wafer. Figure 4.4 c) focuses the gold foil at the bottom of the hole, figure 4.4 d) the

wafer surface. The holes in the wafer have reached the gold foil after about 780 Bosch process iterations. Then another 200 repetitions of the Bosch process were carried out to test the resistance of the thin gold layer at the bottom of the holes. It turns out that the gold foil was chemically and mechanically stable enough not to crack in any of the holes. Therefore, no cracking of the gold thermalization structures which are twice as thick (2 μm) is expected during the fabrication of the detector.

The filling of the etched holes via electroplating has already been developed in [Gam19] and [Sch21], for 300 μm diameter holes which were etched using a cryogenic deep reactive ion etching process. This filling process can now be tested on holes etched using the process developed within the framework of this thesis, to optimize step c) in figure 4.3. The application of the Ag:Er layer (figure 4.3 d)) is an unproblematic standard step which was already done in [Gam19] and[Sch21]. In addition, the exact number of Bosch process repetitions needed to etch 1076 holes with a 300 μm diameter through a 3 inch silicon wafer as specified by the detector design should be determined. Due to the larger amount of material to be etched compared to the 2 inch test wafers, a longer etching process is expected as the amount of radicals in the plasma chamber remains the same.

5. Summary and outlook

Within this thesis a detector was designed for studying dissociative recombination reactions at the cryogenic storage ring CSR of the Max Planck Institute for Nuclear Physics in Heidelberg.

The detector is based on metallic magnetic calorimeters (MMCs). They are well suited for the detection of neutral massive particles and combine an excellent energy resolution with fast signal rise times and behave linearly over a broad energy range. To combine these beneficial properties with a high spatial resolution, the detector developed here features 64×64 MMCs arranged in a square matrix over a $4.48\,\mathrm{cm} \times 4.48\,\mathrm{cm}$ area. Each individual MMC consists of a $698\,\mu\mathrm{m} \times 698\,\mu\mathrm{m}$ large absorber which is thermally connected to a $200\,\mu\mathrm{m} \times 200\,\mu\mathrm{m}$ temperature sensor. The resulting pixel array thus covers the detection area with a filling factor of 99.4 %. In each row 64 MMCs couple to a common detection coil. Pairs of adjacent rows are coupled with different polarities to a common SQUID. Each SQUID thus measures the magnetic flux change summed over a pair of rows, whereby a distinction is made between the two coils, and thus rows, on the basis of the signal polarity. Accordingly, it is possible to assign energy inputs somewhere on the detector with a total of 32 SQUIDs to one of the 64 rows. Each of the 64 temperature sensors within a row is linked to a thermal bath with a slightly different thermal connection. Since the decay time of a temperature increase in a sensor depends directly on this coupling, it is possible to distinguish between the 64 MMCs of each row. In total, it is therefore possible to read out all 4096 pixels of the detector using only 32 SQUIDs without losing spatial information. The detector presented here is the first MMC based detector to implement the discrimination of decay times as part of a readout scheme to reduce spatial complexity.

Since the physical behavior of MMCs is well understood, the energy resolution of the detector can be estimated. Simulations predict an intrinsic energy resolution of $E_{\mathrm{FWHM}} \approx 40\,\mathrm{eV}$ at an operating temperature of 20 mK. This is sufficient to determine the mass of many neutral molecule fragments produced at the CSR with the necessary precision of 1 u.

In addition to the detector design, this thesis discussed its upcoming cleanroom fabrication. In particular, it presented progress in fabricating $300\,\mu\mathrm{m}$ holes through silicon wafers which will subsequently be filled with gold. To this end, the choice of a resist for dry etching of silicon wafers using the Bosch process was optimized.

The featured detector is a successor of the molecular camera "MOCCA" developed in [Gam19] and [Sch21]. Both are based on MMCs and have the same spatial resolution. However, MOCCA uses a different readout scheme. This has the disadvantage that it lowers the theoretically achievable energy resolution of the detector and artificially extends the signal rise times of its MMCs to up to 16 μs, thus potentially limiting time resolution. In addition, MOCCA's design is very complex and susceptible to fabrication errors. In particular, the fabrication of a large number of small sized electrical contacts between conductive layers has proven difficult.

The new detector intends to solve these problems. Its design includes far less electrical contacts, all of which are not problematically small and offers signal rise times of less than 1 μs. However, two new problems may arise. Firstly, it dispenses with a form of redundancy whereby each particle detected by MOCCA generates signals in two independent SQUIDs. Since this is no longer the case here, the detector becomes more vulnerable to falsely detected signals. In addition, this leads to a reduction of its maximum possible measuring rate. The latter is amplified by the second problem: The decay time discrimination provided in the readout scheme is easier with long decay times. However, this parameter also limits the minimum time interval between two measurements at full energy resolution within the same row of the detector. Thus, a trade-off arises here that must be resolved by making the decay times small enough so that the readout scheme just works as intended. In addition, the smallest decay time should not be shorter than 0.5 ms for reasons of energy resolution.

The first prototype of the detector will therefore be built with the decay times presented here between 0.6 and 3.1 ms. If it is easy to distinguish between decay times, the upper value can be lowered later. Since the detector will first be characterized outside the CSR using X-ray sources, the first prototype will have golden absorbers. However, for the later detection of massive particles, more suitable absorber materials should be explored.

In conclusion, the detector could contribute to a better understanding of the chemistry in interstellar clouds due to its unique simultaneous high energetic, temporal and spatial resolution.

A. Appendix

Table A.1: Overview of the length l_i of the gold links to the thermal bath and expected signal decay times τ_i by sensor column. Column number i as in figure 3.1, counted from left to right.

i	l_i $[\mu m]$	τ_i $[ms]$
1	125	3,103
2	123,4	3,064
3	121,8	3,024
4	120,2	2,984
5	118,6	2,944
6	117	2,905
7	115,4	2,865
8	113,8	2,825
9	112,2	2,786
10	110,6	2,746
11	109	2,706
12	107,4	2,666
13	105,8	2,627
14	104,2	2,587
15	102,6	2,547
16	101	2,507
17	99,4	2,468
18	97,8	2,428
19	96,2	2,388
20	94,6	2,349
21	93	2,309
22	91,4	2,269
23	89,8	2,229
24	88,2	2,19
25	86,6	2,15
26	85	2,11
27	83,4	2,071
28	81,8	2,031
29	80,2	1,991
30	78,6	1,951
31	77	1,912
32	75,4	1,872

i	l_i $[\mu m]$	τ_i $[ms]$
33	73,8	1,832
34	72,2	1,792
35	70,6	1,753
36	69	1,713
37	67,4	1,673
38	65,8	1,634
39	64,2	1,594
40	62,6	1,554
41	61	1,514
42	59,4	1,475
43	57,8	1,435
44	56,2	1,395
45	54,6	1,356
46	53	1,316
47	51,4	1,276
48	49,8	1,236
49	48,2	1,197
50	46,6	1,157
51	45	1,117
52	43,4	1,077
53	41,8	1,038
54	40,2	0,998
55	38,6	0,958
56	37	0,919
57	35,4	0,879
58	33,8	0,839
59	32,2	0,799
60	30,6	0,76
61	29	0,72
62	27,4	0,68
63	25,8	0,641
64	24,2	0,601

Table A.2: Overview of the parameters for the cleanroom fabrication of holes in silicon wafers at KIP

Recipe for fabricating holes in silicon with the Bosch process		
HMDS	no	
resist	AZ4562	
spin-coating	step 1:	500 rpm, ramp 6, 7 s
	step 2:	1600 rpm, ramp 6, 30 s
	step 3:	wait 10min at room temperature
softbake	hotplate	100 °C for 3 min
structuring	rehydration	10 min in humid air
	MLA	dose: 550 mJ/cm^2
	develop	AZ726 for 115 s
etching	maschine	Oxford
	recipe	Bosch Etch
	repititions of Bosch process	780 reps for 260 300 μm diameter holes (needs further testing)

Bibliography

[Ban93] S. Bandler, C. Enss, R. Lanou, H. Maris, T. More, F. Porter, and G. Seidel, Metallic magnetic bolometers for particle detection, *Journal of low temperature physics*, **93**(3-4), 709–714, 1993.

[Bru82] J. Bruines, V. de Waal, and J. Mooij, Comment on:"dc squid: Noise and optimization" by tesche and clarke, *Journal of Low Temperature Physics*, **46**(3), 383–386, 1982.

[Bur08] A. Burck, Entwicklung großflächiger mikrostrukturierter magnetischer Kalorimeter mit Au: Er-und Ag: Er-Sensoren für den energieaufgelösten Nachweis von Röntgenquanten und hochenergetischen Teilchen, PhD Thesis, 2008.

[Cam10] J. Cami, J. Bernard-Salas, E. Peeters, and S. E. Malek, Detection of c60 and c70 in a young planetary nebula, *Science*, **329**(5996), 1180–1182, 2010.

[DG17] S. De Graaf, A. Adamyan, T. Lindström, D. Erts, S. Kubatkin, A. Y. Tzalenchuk, and A. Danilov, Direct identification of dilute surface spins on al 2 o 3: Origin of flux noise in quantum circuits, *Physical review letters*, **118**(5), 057703, 2017.

[DW75] H. De Waard, The investigation of radiation damage and lattice location by nuclear hyperfine interaction techniques, *Physica Scripta*, **11**(3-4), 157, 1975.

[Ens00] C. Enss and S. Hunklinger, Low-temperature physics; Tieftemperaturphysik, Springer, 2000.

[Fle00] A. Fleischmann, J. Schönefeld, J. Sollner, C. Enss, J. Adams, S. Bandler, Y. Kim, and G. Seidel, Low temperature properties of erbium in gold, *Journal of low temperature physics*, **118**(1), 7–21, 2000.

[Fle03] A. Fleischmann, Magnetische Mikrokalorimeter: Hochauflösende Röntgenspektroskopie mit energiedispersiven Detektoren, PhD Thesis, Ruprecht-Karls-Universität Heidelberg, 2003.

[Fle05] A. Fleischmann, C. Enss, and G. Seidel, Metallic magnetic calorimeters, *Cryogenic particle detection*, 151–216, 2005.

[Fle09] A. Fleischmann, L. Gastaldo, S. Kempf, A. Kirsch, A. Pabinger, C. Pies, J.-P. Porst, P. Ranitzsch, S. Schäfer, F. v. Seggern, et al., Metallic magnetic calorimeters, in *AIP Conference Proceedings*, Volume 1185, 571–578, American Institute of Physics, 2009.

[Fra76] S. Fraga, J. Karwowski, and K. Saxena, Handbook of atomic data elsevier, *New York*, 1976.

[Gam17] L. Gamer, C. E. Düllmann, C. Enss, A. Fleischmann, L. Gastaldo, C. Hassel, S. Kempf, T. Kieck, and K. Wendt, Simulation and optimization of the implantation of holmium atoms into metallic magnetic microcalorimeters for neutrino mass determination experiments, *Nuclear Instruments and Methods in Physics Research Section A: Accelerators, Spectrometers, Detectors and Associated Equipment*, **854**, 139–148, 2017.

[Gam19] L. Gamer, Entwicklung und Charakterisierung des 4k-Pixel Detektorarrays MOCCA für die energie- und ortsaufgelöste Detektion neutraler Molekülfragmente, PhD Thesis, Ruprecht-Karls-Universität Heidelberg, 2019.

[Gas17] L. Gastaldo, K. Blaum, K. Chrysalidis, T. D. Goodacre, A. Domula, M. Door, H. Dorrer, C. E. Düllmann, K. Eberhardt, S. Eliseev, et al., The electron capture in 163 ho experiment–echo, *The European Physical Journal Special Topics*, **226**(8), 1623–1694, 2017.

[Gei20] J. Geist, Bestimmung der Isomerenergie von 229Th mit dem hochauflösenden Mikrokalorimeter-Array maXs30, PhD Thesis, Ruprecht-Karls-Universität Heidelberg, 2020.

[Hah92] W. Hahn, M. Loewenhaupt, and B. Frick, Crystal field excitations in dilute rare earth noble metal alloys, *Physica B: Condensed Matter*, **180**, 176–178, 1992.

[Hen17] D. Hengstler, Development and characterization of two-dimensional metallic magnetic calorimeter arrays for the high-resolution X-ray spectroscopy, PhD Thesis, Ruprecht-Karls-Universität Heidelberg, 2017.

[Her21] M. Herbst, A. Fleischmann, and C. Enss, Thermodynamic properties of silver erbium alloys for use in metallic magnetic calorimeters, *Journal of Low Temperature Physics*, to be released 2021.

[Hun17] S. Hunklinger, Festkörperphysik, De Gruyter Oldenbourg, 2017.

[Kas56] T. Kasuya, A theory of metallic ferro-and antiferromagnetism on zener's model, *Progress of theoretical physics*, **16**(1), 45–57, 1956.

[Kem16] S. Kempf, A. Ferring, and C. Enss, Towards noise engineering: Recent insights in low-frequency excess flux noise of superconducting quantum devices, *Applied Physics Letters*, **109**(16), 162601, 2016.

[Kem18] S. Kempf, A. Fleischmann, L. Gastaldo, and C. Enss, Physics and applications of metallic magnetic calorimeters, *Journal of Low Temperature Physics*, **193**(3), 365–379, 2018.

[Koc07] R. H. Koch, D. P. DiVincenzo, and J. Clarke, Model for 1/f flux noise in squids and qubits, *Physical review letters*, **98**(26), 267003, 2007.

[Kog81] S. M. Kogan, 1f noise in spin glasses and in the disordered kinetic ising model, *Solid State Communications*, **38**(11), 1015–1018, 1981.

[Kum16] P. Kumar, S. Sendelbach, M. Beck, J. Freeland, Z. Wang, H. Wang, C. Y. Clare, R. Wu, D. Pappas, and R. McDermott, Origin and reduction of 1/f magnetic flux noise in superconducting devices, *Physical Review Applied*, **6**(4), 041001, 2016.

[McG18] B. A. McGuire, 2018 census of interstellar, circumstellar, extragalactic, protoplanetary disk, and exoplanetary molecules, *The Astrophysical Journal Supplement Series*, **239**(2), 17, 2018.

[Pie12] C. Pies, maXs-200: Entwicklung und Charakterisierung eines Röntgendetektors basierend auf magnetischen Kalorimetern für die hochauflösende Spektroskopie hochgeladener Ionen, PhD Thesis, Ruprecht-Karls-Universität Heidelberg, 2012.

[Por14] J.-P. Porst, S. Bandler, J. Adams, M. Balvin, S. Busch, M. Eckart, R. Kelley, C. Kilbourne, S. Lee, P. Nagler, et al., Characterization and performance of magnetic calorimeters for applications in x-ray spectroscopy, *Journal of Low Temperature Physics*, **176**(5), 617–623, 2014.

[Rud54] M. A. Ruderman and C. Kittel, Indirect exchange coupling of nuclear magnetic moments by conduction electrons, *Physical Review*, **96**(1), 99, 1954.

[Sch00] J. Schönefeld, Entwicklung eines mikrostrukturierten magnetischen Tieftemperatur-Kalorimeters zum hochauflösenden Nachweis von einzelnen Röntgenquanten, PhD Thesis, Ruprecht-Karls-Universität Heidelberg, 2000.

[Sch15] D. Schulz, Entwicklung einer 4k-pixel-molekülkamera, basierend auf magnetischen mikrokalorimetern, für den energie- und ortsaufgelösten nachweis von neutralen molekülfragmenten, 2015.

[Sch19] C. D. Schötz, PolarmaXs: hochauflösendes, polarisationssensitives Röntgenspektrometer basierend auf magnetischen Mikrokalorimetern, PhD Thesis, Universität Heidelberg, 2019.

[Sch21] D. Schulz, Development and characterization of MOCCA, a 4k-pixel molecule camera for the energy-resolved detection of neutral molecule fragments, PhD Thesis, Ruprecht-Karls-Universität Heidelberg, 2021.

[Sik20] T. Sikorsky, J. Geist, D. Hengstler, S. Kempf, L. Gastaldo, C. Enss, C. Mokry, J. Runke, C. E. Düllmann, P. Wobrauschek, et al., Measurement of the th 229 isomer energy with a magnetic microcalorimeter, *Physical Review Letters*, **125**(14), 142503, 2020.

[Tao71] L. Tao, D. Davidov, R. Orbach, and E. Chock, Hyperfine splitting of er and yb resonances in au: A separation between the atomic and covalent contributions to the exchange integral, *Physical Review B*, **4**(1), 5, 1971.

[Tes77] C. D. Tesche and J. Clarke, Dc squid: Noise and optimization, *Journal of Low Temperature Physics*, **29**(3), 301–331, 1977.

[Tie05] A. G. Tielens, The physics and chemistry of the interstellar medium, Cambridge University Press, 2005.

[Vel19] C. Velte, Measurement of a high energy resolution and high statistics 163Ho electron capture spectrum for the ECHo experiment, PhD Thesis, Ruprecht-Karls-Universität Heidelberg, 2019.

[Wil69] G. Williams and L. Hirst, Crystal-field effects in solid solutions of rare earths in noble metals, *Physical Review*, **185**(2), 407, 1969.

[Yos57] K. Yosida, Magnetic properties of cu-mn alloys, *Physical Review*, **106**(5), 893, 1957.

[Zha11] Y. Zhang and S. Kwok, Detection of c60 in the protoplanetary nebula iras 01005+ 7910, *The Astrophysical Journal*, **730**(2), 126, 2011.

Acknowledgements

Abschließend möchte ich mich bei all denen bedanken, die zum Gelingen dieser Arbeit beigetragen haben. Mein Dank gilt im Besonderen:

Prof. Dr. Christian Enss für die Möglichkeit in seiner Arbeitsgruppe an einem interessanten Thema forschen zu dürfen,

Priv. -Doz. Dr. Loredana Gastaldo für die Übernahme des Zweitgutachtens dieser Arbeit, den von ihr ausgestrahlten ansteckenden Enthusiasmus bezüglich des Themas und ihre warme Art durch die man sich schnell in der Arbeitsgruppe heimisch fühlt,

Dr. Andreas Fleischmann für seine Betreuung, sowie seine Funktion als wandelndes Lexikon für Tieftemperaturdetektoren und die daraus resultierenden vielen sehr aufschlussreichen Diskussionen über den Inhalt der Arbeit und diverse sonstige physikalische Sachverhalte,

Dr. Lisa Gamer für ihr immer offenes Ohr für Fragen, viele thematische Anregungen und Ideen, sowie das Korrekturlesen dieser Arbeit,

Dr. Dennis Schulz für die Einführung in das Thema und viele beantwortete Fragen bezüglich MOCCA, sowie seine erfolgreichen Bemühungen mich während der Pandemie in die Arbeitsgruppe einzubinden,

Christian Ständer für die nächtliche Unterstützung bei der Bedienung des Kryostaten und des Bond Geräts,

Meinen Eltern für 24 Jahre intensiver Förderung die mich an diesen Punkt gebracht haben, sowie ihre inhaltlichen und grammatikalischen Anregungen beim Schreiben dieser Arbeit,

Arnulf Barth, Dr. Andreas Reifenberger, Christopher Jakob, Matthew Herbst und allen anderen Mitgliedern von F4 und F3 für viele spannende Diskussionen, die nie langweilige Zeit im Büro und beim Mittagessen und ein generell sehr angenehmes Arbeitsumfeld.

Ich versichere, dass ich diese Arbeit selbständig verfasst und keine anderen als die angegeben Quellen und Hilfsmittel benutzt habe.

Heidelberg, den 10.11.2020 .....

(Ansgar Lowack)